



Structural basis of rhodopsin/G protein coupling : biochemical activity of peptide complexes, photo cross-linking, and mass spectrometric analysis  
by Paul Camille Kraft

A dissertation submitted in partial fulfillment of the requirements for the degree Of Doctor of Philosophy In Biochemistry  
Montana State University  
© Copyright by Paul Camille Kraft (2001)

**Abstract:**

Physiological and sensory mechanisms are primarily controlled by membrane impermeant signals—which are usually detected by membrane-spanning receptor proteins that ultimately trigger intracellular responses. Similarly, development and repair in multi-cellular organisms are controlled by specific adhesion mechanisms that recognize macromolecular binding sites outside cells and control cytoplasmic responses. Understanding of signaling and adhesion mechanisms could be greatly advanced if the structures of the membrane-spanning receptor proteins and their non-covalent interaction partners could be determined at atomic resolution—but these structures can not typically be deduced by x-ray crystallography or NMR.

Mass spectrometry is able to mass analyze high molecular weight species, however, non-covalent protein-ligand or protein-protein interactions are disrupted by the non-aqueous conditions used in conventional mass spectrometry. This thesis describes new mass spectrometric methodologies to analyze proteins directly from aqueous solutions, which is an important first step in mass spectrometry of non-covalent protein-ligand complexes. Insight is gained into fundamental mechanisms of laser desorption ionization mass spectrometry from aqueous solutions.

This thesis also describes biochemical and mass spectrometric methods to identify non-covalent interactions between the rhodopsin visual receptor and the G protein, transducin. The contacts between rhodopsin and transducin were studied using synthetic peptides derived from transducin that were characterized by their ability to inhibit rhodopsin catalysis of nucleotide binding by transducin. The peptides were also characterized for their ability to inhibit the homologous formyl peptide receptor's catalysis of nucleotide binding by the Gi protein.

Fluorescent photo-activatable analogs of the most potent peptides were synthesized. Non-covalent rhodopsin-peptide interactions were tested for specificity and covalently stabilized by photo-chemical cross-linking. Rhodopsin-peptide complexes (which are about 42,000 Da) must be cleaved into smaller peptides for mass spectrometric analysis of the amino acid sites cross-linked. Cyanogen bromide cleavage of rhodopsin reduced the size of the hydrophobic fragments to facilitate analysis.

Methods are described for mass spectral analysis of all of the cyanogens bromide fragments of rhodopsin at the picomole level, which is an essential first step in identifying the peptide cross-linking sites in rhodopsin. These results represent significant progress in efforts to define the molecular contacts between rhodopsin and transducin and homologous proteins.

STRUCTURAL BASIS OF RHODOPSIN/G PROTEIN COUPLING:  
BIOCHEMICAL ACTIVITY OF PEPTIDE COMPLEXES, PHOTO CROSS-  
LINKING, AND MASS SPECTROMETRIC ANALYSIS

By

Paul Camille Kraft

A dissertation submitted in partial fulfillment of the requirements for the degree

Of

Doctor of Philosophy

In

Biochemistry

MONTANA STATE UNIVERSITY  
Bozeman, Montana

April 2001

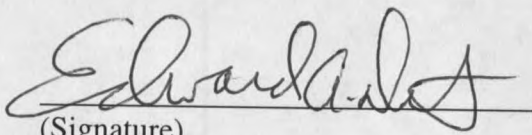
D378  
K8557

APPROVAL

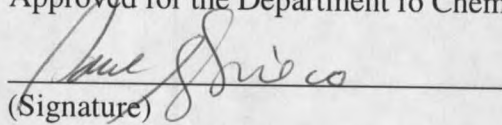
Of a dissertation submitted by

Paul Camille Kraft

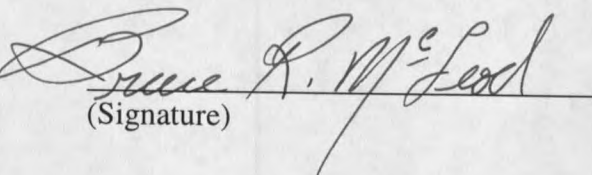
This dissertation has been read by each member of the dissertation committee and has been found to be satisfactory regarding content, English usage, format, citations, bibliographic style, and consistency, and is ready for submission to the College of Graduate Studies.

Edward A. Dratz  4/23/2001  
(Signature) Date

Approved for the Department fo Chemistry and Biochemistry

Paul Grieco  4/23/01  
(Signature) Date

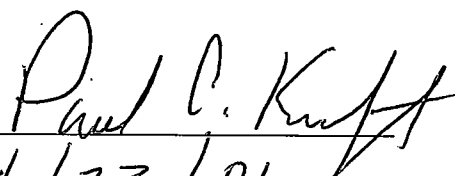
Approved for the College of Graduate Studies

Bruce McLeod  5-2-01  
(Signature) Date

## STATEMENT OF PERMISSION TO USE

In presenting this thesis in partial fulfillment of the requirements for a doctoral degree at Montana State University, I agree that the library shall make it available to the borrowers under the rules of the Library. I further agree that copying of this thesis is allowable only for scholarly purposes, consistent with "fair use" as prescribed in the U.S. Copyright Law. Requests for extensive copying or reproduction of this thesis should be referred to Bell & Howell Information and Learning, 300 North Zeeb Road, Ann Arbor Michigan 48106, to whom I have granted "the exclusive right to reproduce and distribute my thesis in and from microform along with the non-exclusive right to reproduce and distribute my abstract in any format in whole or in part".

Signature



Date

4/23/01

## ACKNOWLEDGEMENTS

Thanks to Prof. Edward Dratz, Prof. Jan Sunner, Dr. John Mills, Prof. Sergey Alimpiev, Prof. Heidi Hamm, Dr. Heini Miettinen, Blaine Roberts, and Dr. Joseph Sears.

I would also like to thank my parents, Ken & Anna Kraft, family, friends, and last but certainly not least, Lara Taubner, the love of my life.

## TABLE OF CONTENTS

	Page
1. INFRARED LASER DESORPTION IONIZATION MASS SPECTROMETRY ON FROZEN AQUEOUS SOLUTIONS OF PROTEINS AND PEPTIDES	
Abstract.....	1
Introduction.....	2
Experimental.....	6
Results and Discussion.....	14
Cryo-IR-SALDI mass spectra of peptides.....	15
Comparison between different SALDI solids for protein Desorption.....	18
UV-laser irradiation of cryo-SALDI samples.....	20
Laser "drilling" experiments and surface charging.....	23
Larger proteins and clustering.....	25
Results from aqueous solutions with no cryoprotectant added.....	28
Multiple Charging.....	30
Ionization processes.....	31
Conclusions.....	39
2. REVIEW OF LITERATURE AND METHODS USED TO STUDY RHODOPSIN/TRANSDUCIN INTERACTIONS..... 41	
Description of Signal Transduction in a Rod Outer Segment Cell.....	41
Relationship of Rhodopsin/Transducin System to other GPCR/G Protein Systems.....	43
Rhodopsin dark structure and homology to other GPCRs.....	43
Transducin structure and homology to other G proteins.....	50
Methods to Study Signal Transduction.....	54
Spectral Characteristics of the Rhodopsin/Transducin System.....	56
Constitutive Activity of Rhodopsin and Transducin.....	59
Role of Retinal in maintaining low basal rhodopsin activity.....	60
Role of rhodopsin residues in maintaining its low basal activity.....	61
Role of transducin residues in maintaining its low basal activity.....	64
Activation of Rhodopsin and Transducin.....	66
Retinal activation of rhodopsin.....	66

Role of rhodopsin residues in activation.....	68
Role of transducin residues involved in activation/coupling to rhodopsin.....	71
Peptides as Probes of GPCR and G Protein Function.....	72
3. PROBING NON-COVALENT INTERACTIONS BETWEEN RHODOPSIN AND TRANSDUCIN BY PEPTIDE INHIBITION OF RHODOPSIN-CATALYZED NUCLEOTIDE EXCHANGE, AND CROSS-LINKING PHOTO ACTIVATABLE PEPTIDE ANALOGS TO RHODOPSIN.....	78
Abstract.....	78
Introduction.....	79
Materials and Methods.....	81
Results.....	84
Discussion.....	100
4. MASS SPECTROMETRIC ANALYSIS OF CYANOGEN BROMIDE FRAGMENTS OF INTEGRAL MEMBRANE PROTEINS AT THE PICOMOLE LEVEL: APPLICATION TO RHODOPSIN.....	109
Abstract.....	109
Introduction.....	110
Materials and Methods.....	112
Results.....	114
Discussion.....	127
Conclusion.....	130
Acknowledgements.....	130
5. CONCLUSIONS AND FUTURE WORK.....	131
Preservation of non-covalent complexes in laser desorption Experiments.....	131
Defining the amino acid molecular contacts between rhodopsin and Transducin.....	135
REFERENCES.....	148

## LIST OF TABLES

Table	Page
1. Summary of cryo-IR-SALDI results for selected solids additives.....	21
2. Characteristics of Transducin alpha subunit C-terminal peptide Analog.....	85
3. Peptide masses matched to within 0.05% of the masses expected for the cyanogen bromide digest of rhodopsin.....	124

## LIST OF FIGURES

Figure	Page
1. Cryo-IR-SALDI mass spectrum of 0.9mM angiotensin II in 67% glycerol in water.....	17
2. Abundances, as determined by peak heights, of singly protonated nicotinic acid (NH <sup>+</sup> ) and singly protonated angiotensin II (AH <sup>+</sup> ) ions as a function of laser pulse energy using the same experimental conditions as Figure 1.....	19
3. Cryo-IR-SALDI mass spectra of equimolar mixture of 0.5mM myoglobin ("M") and cytochrome c ("C") in a 67% glycerol water solution with different SALDI solids added.....	22
4. Nicotinic acid cryo-IR-SALDI mass spectrum of 0.05 mM lactic dehydrogenase ("I") and 0.10 mM cytochrome c ("C") in water:ethanol:glycerol (25:25:50, v:v:v).....	27
5. Nicotinic acid cryo-IR-SALDI mass spectrum of 0.34 bovine serum albumin ("B", 66,430 Da) in glycerol/water.....	29
6. Thymine cryo-IR-SALDI mass spectrum of 0.1mM myoglobin ("M") in 67% glycerol in water .....	33
7. The light stimulated signal transduction cascade. Also shown are depictions of the location of rhodopsin in the rod cell, the cis to trans isomerization of retinal, and the hydrolysis of cyclic GMP.....	42
8. GPCR Evolution Tree.....	44
9. Relationships among mammalian G protein alpha subunits.....	45
10. A. Snake Diagram of Rhodopsin .....	46
10. B. Ribbon model of the crystal structure of dark-adapted rhodopsin.....	47
11. Muscarinic receptors M4 & M2 couple to Gi/o, and M5, M3; & M1 couple to Gq. Snake diagram below indicates 24 positions near the cytoplasmic side that Horn et al correlated with G protein selectivity.....	49
12. Sequence of the alpha subunit Gi chimera of transducin.....	51
13. A. Backbone trace of heterotrimeric transducin Gi chimera that was crystallized by Lambright et al [Nature 1996].....	52
13. B. Expanded view of transducin Gi chimeric alpha subunit.....	53
14. GTPγS35 filter binding inhibition assay.....	57
15. Extra Meta II assay.....	58
16. Spectrophotometrically detected intermediates in the Photoisomerization of Rh.....	62
17. Structural analysis of A326S Gi alpha-1 (95) .....	67

18. A summary of 340-350 peptide analogs tested for their abilities to stabilize metarhodopsin II (EC50) and for their abilities to inhibit a340-350 K341R peptide fusion protein (IC50), as measured by ELISA.....	75
19. Summary of 340-350 peptide analogs tested for their abilities to stabilize metarhodopsin II (EC50), (149).....	76
20A&B. Fluorescent peptide-2 cross-linking experiments.....	88
20.C. SDS-PAGE confirmation of cross-linking specificity.....	89
21. Circular dichroism analysis of transducin 340-350 peptide.....	90
22. Comparison of Unihibited, N-acetyl-VLEDLRSCGLF, and N-acetyl-311-329-amide inhibited GTP-gamma-35S binding in urea washed ROS with exogenous transducin added.....	93
23. Ribbon and tube model of Heterotrimer G protein, transducin with expanded view of residues 311-342.....	94
24. Sequence alignment of the C-terminus's of Gi1, Gt, and Gs.....	95
25. Agonist formyl-MLF stimulated human formyl peptide receptor Catalyzed GTP- $\gamma$ -S35 binding by transducin.....	97
26. Ac311-329NH2 titration of agonist formyl-MLF stimulated human FPR catalyzed GTP- $\gamma$ -S35 binding by Gi2.....	98
27. Peptide inhibition of urea washed (Gt depleted) bovine rhodopsin catalyzed GTP-gamma-S35 binding by exogenous Gi/o.....	99
28. Transmembrane topological model of rhodopsin.....	115
29. SDS-PAGE analysis of fluoroscein labeled proteins and peptides.....	118
30. Delayed extraction and reflected MALDI spectrum spectrum of 2 picomole of reduced and thiol alkylated rhodopsin cyanogen bromide digest in ACHA.....	120
31. Unsmoothed (to clearly display monoisotopic resolution of the insets) reflected and delayed extraction MALDI spectrum of 4 picomole of reduced and thiol alkylated rhodopsin cyanogen bromide in ACHA.....	122
32. Linear mode, delayed extraction MALDI spectrum of 4 picomole of reduced and thiol alkylated rhodopsin cyanogen bromide digest in 2,5-dihydroxybenzoic acid.....	125
33. MALDI post source decay (PSD) spectrum of fragment 310-317.....	126
34. Flow chart of cross-link isolation.....	137
35A. Fluorescence image of tris/tricine gel of cyanogen bromide digest of peptide-2 cross-linked to rhodopsin.....	139
35B. Fluorescence and Coomassie stain image of the same tris/tricine gel of Lys-C digestion of peptide-2 cross-linked to rhodopsin.....	142

ABSTRACT

Physiological and sensory mechanisms are primarily controlled by membrane impermeant signals—which are usually detected by membrane-spanning receptor proteins that ultimately trigger intracellular responses. Similarly, development and repair in multi-cellular organisms are controlled by specific adhesion mechanisms that recognize macromolecular binding sites outside cells and control cytoplasmic responses. Understanding of signaling and adhesion mechanisms could be greatly advanced if the structures of the membrane-spanning receptor proteins and their non-covalent interaction partners could be determined at atomic resolution—but these structures can not typically be deduced by x-ray crystallography or NMR.

Mass spectrometry is able to mass analyze high molecular weight species, however, non-covalent protein-ligand or protein-protein interactions are disrupted by the non-aqueous conditions used in conventional mass spectrometry. This thesis describes new mass spectrometric methodologies to analyze proteins directly from aqueous solutions, which is an important first step in mass spectrometry of non-covalent protein-ligand complexes. Insight is gained into fundamental mechanisms of laser desorption ionization mass spectrometry from aqueous solutions.

This thesis also describes biochemical and mass spectrometric methods to identify non-covalent interactions between the rhodopsin visual receptor and the G protein, transducin. The contacts between rhodopsin and transducin were studied using synthetic peptides derived from transducin that were characterized by their ability to inhibit rhodopsin catalysis of nucleotide binding by transducin. The peptides were also characterized for their ability to inhibit the homologous formyl peptide receptor's catalysis of nucleotide binding by the Gi protein.

Fluorescent photo-activatable analogs of the most potent peptides were synthesized. Non-covalent rhodopsin-peptide interactions were tested for specificity and covalently stabilized by photo-chemical cross-linking. Rhodopsin-peptide complexes (which are about 42,000 Da) must be cleaved into smaller peptides for mass spectrometric analysis of the amino acid sites cross-linked. Cyanogen bromide cleavage of rhodopsin reduced the size of the hydrophobic fragments to facilitate analysis. Methods are described for mass spectral analysis of all of the cyanogens bromide fragments of rhodopsin at the picomole level, which is an essential first step in identifying the peptide cross-linking sites in rhodopsin. These results represent significant progress in efforts to define the molecular contacts between rhodopsin and transducin and homologous proteins.

## CHAPTER 1

INFRARED LASER DESORPTION IONIZATION  
MASS SPECTROMETRY ON FROZEN AQUEOUS  
SOLUTIONS OF PROTEINS AND PEPTIDESAbstract

Surface-assisted, laser desorption ionization (SALDI) time-of-flight mass spectra of proteins and peptides have been obtained from bulk frozen aqueous solutions by adding solid organic powders to the solutions before freezing. Abundant analyte ions were obtained with a 3.28  $\mu\text{m}$  Nd:YAG/OPO laser. Twenty compounds were evaluated as solid additives, and sixteen yielded protein mass spectra. Successful solids included compounds like pyrene, aspartic acid, and polystyrene. The best results were obtained with nicotinic acid and indole-2-carboxylic acid, which yielded protein mass spectra anywhere on the sample and with every laser shot. Compared with UV-MALDI on the same instrument, cryo-IR-SALDI had a comparable detection limit ( $\approx 1 \mu\text{M}$ ), a lower mass resolution for peptides, and a higher mass resolution for large proteins. Approximately 2,500 cryo-IR-SALDI mass spectra were obtained from a single spot on a 0.3 mm thick frozen sample before the metal surface was reached. About 0.1 nL of frozen solution was desorbed per laser shot. The extent of protein charging varied between the SALDI solids used. With thymine, myoglobin charge states up to  $\text{MH}_{12}^{+12}$  were observed. It is tentatively concluded that observed ions are pre-formed in the frozen sample.

### Introduction

Matrix-assisted laser desorption ionization mass spectrometry (MALDI-MS) is a powerful and widely used method for the analysis of large biochemical molecules [1,2]. In MALDI, the biomolecules are entrained into crystals of a UV-absorbing matrix by solvent evaporation [3]. Irradiation of the sample with a short pulse from a UV laser results in the desorption and ionization of the biomolecules. Together with electrospray [4], MALDI has revolutionized biochemical mass spectrometry.

The goal of performing laser desorption mass spectrometry of biomolecules directly from water solutions has been pursued over several years for a number of reasons. 1) Aqueous solutions constitute the native environment for most biomolecules, and analysis of biomolecules directly from aqueous solutions would require a minimum of sample manipulations. 2) A sample preparation method that uses a water matrix might work equally well for a wide range of biomolecules. Presently, a number of different matrices are used in MALDI, and finding the best matrix and sample preparation method for a given analyte is partly a matter of trial and error. 3) UV-MALDI is sometimes troubled with a wide range of sensitivities for components in mixtures and widely varying signal intensities at different spots on the sample surface. A desorption method with a more uniform and predictable sensitivity would be extremely useful. 4) An aqueous environment is usually necessary to maintain the structure of, and interactions between, most proteins and other biomolecules (although aqueous glycerol is a fairly mild solvent.) Thus, mass spectra of macromolecules in conformations competent to form native intermolecular complexes, as well as the intact

complexes of these molecules, are best obtained directly from aqueous solutions. In MALDI, analytes are subjected to drying in concentrated, usually acidic, organic matrix solutions and to the formation of matrix crystals. During this process, there will be a strong tendency for most biomolecules to denature, and this may well explain why the dissociated subunits of complex proteins are typically seen in MALDI mass spectra. Suitable freezing protocols are able to maintain the native, functional conformation of most protein systems [5,6]. Progress in desorbing macromolecules from frozen aqueous solutions may lead to methods for the reliable and sensitive detection of intact subunit proteins and other non-covalent complexes by laser desorption mass spectrometry. 5) If laser desorption could be performed directly from frozen aqueous solutions, the localized *in situ* detection of proteins and other biomolecules from intact frozen cells and tissues might become possible.

Considering the perceived desirable desorption properties above, it is unfortunate that it has proven to be extremely difficult to obtain gas-phase ions of biomolecules by laser desorption from frozen water ice solutions [7,8]. This situation also represents a challenge to our understanding of desorption/ionization processes.

Presently, UV lasers are almost exclusively used for MALDI mass spectrometry. Nitrogen lasers at 337 nm and Nd:YAG laser harmonics at 266 or 355 nm are common. Water, glycerol, and most organic solvents do not absorb at these wavelengths. However, water and other hydroxylated solvents have strong absorption bands in the IR, near 3  $\mu\text{m}$  [9]. A number of publications have appeared that deal with IR laser desorption mass spectrometry [10-16] and with laser desorption from water and hydroxylated solvents [10,17]. Glycerol

was used as a matrix in the early work by Tanaka et al. [17] who obtained protein mass spectra by using 300 Å diameter cobalt particles to couple the laser energy into the liquid.

Hillenkamp et al. demonstrated IR-MALDI using a 2.94 μm Q-switched Er:YAG laser with a 150 ns pulse width [10]. Protein mass spectra were obtained from several MALDI matrices. However, a spectrum of lysozyme (14 kDa) using a liquid glycerol matrix was also reported [10]. The authors later obtained very similar results when using a pulsed 10.6 μm CO<sub>2</sub> laser [11]. In a recent paper, Hillenkamp et al. reported mass spectra of a range of proteins using glycerol as the matrix [15]. IR-MALDI was reported to have a higher upper mass limit and a higher mass resolution for large proteins than UV-MALDI on the same samples [12,15,18]. Metastable fragmentation of larger proteins, above about 20 kDa, was found to be much less of a problem with IR-MALDI [15]. On the other hand, IR-MALDI consumed much more material than UV-MALDI, and only a few spectra could be obtained from the same spot on the desorption probe in IR-MALDI [11,13,15]. This was explained by a large neutral yield with an ablation depth of 0.1 to 0.5 μm in the thin, dry samples employed. Biemann et al. have also demonstrated applications of IR-MALDI to dry samples [19,20], and the application of a Cr:LiSAF pumped OPO laser to IR-MALDI was recently demonstrated [21].

The characteristics of liquid water ablation, induced by high fluence IR laser pulses have been studied (see [22] and references therein). Several factors, including changes in the absorption coefficient of water during the laser pulse [23], the development of shock waves, and delayed ablation have been shown to be important to the dynamics of laser-induced

ablation of water and biological materials with a high water content [22,24]. Of particular relevance to the present work are previous reports of laser desorption of biomolecules, with and without mass spectrometry, from frozen aqueous solutions. Williams et al. reported successful desorption of nucleic acid oligomers by laser ablation from films of frozen aqueous solutions where the water content had been reduced by sublimation in vacuum, such that the film had a total thickness of a few micrometers [7,25-27]. A visible wavelength laser beam from a tunable dye laser heated the underlying copper substrate surface. The reproducibility of ionization was, however, reported to be a problem in these experiments [27,28]. Becker et al. have demonstrated advantages of adding photoabsorbing substituted phenols to frozen films containing DNA [29].

Recently, Hillenkamp et al. demonstrated IR-MALDI mass spectra of proteins from air-dried films of protein solutions. In order to retain residual water in the films, they were frozen before being introduced into the vacuum [8]. An Er:YAG laser (2.94  $\mu\text{m}$ , 150 ns pulse length) was used for these experiments. A mass spectrum was obtained only with the first laser shot, from any one single sample spot. Protein spectra had a rather high mass resolution, in the 300 to 350 range. The upper mass limit was reported to be 30 kDa, with a higher mass limit of 70 kDa if TrisHCl, a known IR MALDI matrix, was added to the aqueous solution [8]. Protein spectra were also reported from a hen egg lysozyme crystal. The authors emphasized that no protein spectra had been obtained from the bulk frozen, aqueous solutions, despite extensive efforts to vary experimental conditions [8].

Alimpiev et al. have used CO<sub>2</sub> lasers for ablation of frozen aqueous solutions. They used a tunable UV laser to ionize desorbed organic molecules by time-delayed, resonance-enhanced, multi-photon post-ionization [30-32]. The method was successful for ultra-high sensitivity detection of simple organic molecules, such as aromatic amino acids and phenol, dissolved in water. However, the upper mass limit of the method was found to be low and was limited by fragmentation of the analyte molecules by the UV and IR lasers.

Recently, we introduced the use of carbon powder suspensions in liquid glycerol as a matrix for laser desorption ionization at room temperature [33], and we refer to this method as Surface-Assisted Laser Desorption Ionization (SALDI) Mass Spectrometry. Graphite SALDI/MS has been applied also to frozen water solutions, as reported at a recent conference [34]. Using the 3.28  $\mu\text{m}$  Nd:YAG/OPO laser, we found that spectra of organic molecules and peptides were easily and reliably obtained. However, with carbon powders we were not successful in obtaining mass spectra of proteins larger than about 20,000 Da. In the present work, we present a SALDI method that uses suspensions of organic crystals, instead of the carbon powder, in frozen, aqueous solutions for cryo-IR-SALDI. This cryo-IR-SALDI MS method reliably produces intense peptide and protein ion signals.

### Experimental

Experiments were performed on a modified VESTEC 2000, 1.35 m linear time-of-flight mass spectrometer (Perceptive Biosystems, Framingham, MA). The acceleration voltage was 20,000 V, and all spectra were obtained in positive ion mode. A guide-wire

along the center of the flight tube was suspended from a point 6" from the beginning of the field-free region to a point 2" in front of the ion detector. The guide wire was normally held at -120 V. Unless otherwise noted, the guide wire was used as a low mass gate by switching the guide-wire voltage to +120 V for 3.0  $\mu$ s after the laser pulse. Time-of-flight mass spectra were recorded on a Tektronix TDS520 storage oscilloscope and downloaded onto a PC for analysis. Internal mass calibration was used.

The tip of a 1/4" stainless steel insertion probe consisted of a copper rod with a 5.0 mm diameter front sample loading surface. This surface was flush with the "sample electrode" surface during desorption. The insertion probe tip made both thermal and electrical contact with the sample electrode plate, and both were maintained at the full acceleration voltage. Two additional electrodes defined the extraction electric field. The first acceleration electrode had a 1/4" central hole, was positioned 0.5" from the sample electrode, and was maintained at half the full acceleration voltage. A second acceleration electrode had a 1/4" central hole covered with a fine wire mesh, was positioned 1.0" from the sample electrode, and was kept at ground potential. With a 20,000 V acceleration voltage, the ion extraction field was  $7.9 \times 10^3$  V/cm.

The sample electrode was cooled by means of a cold-finger. An electrically insulating BeO ceramic rod was attached to the sample plate. BeO was used because its heat conductivity at low temperature is significantly higher than that of other common electrical insulators [35]. A copper rod was soldered to a stainless steel vacuum feedthrough. Inside the vacuum chamber, the copper rod was connected to a copper holder of the BeO rod by

means of a flexible, braided copper strap. Outside the vacuum chamber, the copper rod dipped into a liquid-nitrogen-filled Dewar. One end of a 1/4" diameter aluminum garnet rod was also attached to the sample electrode, and a thermocouple was glued to the other end with epoxy. The temperature of the electrode was monitored with a Fluke 52 digital thermometer (John Fluke, Palantine, IL). Approximately 45 minutes after filling the Dewar with liquid nitrogen, the sample electrode temperature stabilized at about -140°C. A TV camera (Watec 902, Edmund Scientific) was aimed through a view-port at the top of the ion source chamber, and the sample surface was viewed with 19x magnification on a TV monitor.

The mass spectrometer was equipped with a Nd:YAG/OPO IR laser with a fixed wavelength of 3.28  $\mu\text{m}$  (Big Sky Laser, Bozeman, MT). A maximum of about 200 mJ of a 1.064  $\mu\text{m}$  laser pulse from the Nd:YAG laser (model CFR 400) was used to pump a double-pass, KTP OPO crystal. The crystal was used in a non-critically phase matched condition (90° phase matching) to give a signal beam at 1.57  $\mu\text{m}$  and an idler beam at 3.28  $\mu\text{m}$ . A dichroic mirror was used to reflect the signal beam out of the idler beam path. The 3.28  $\mu\text{m}$  IR beam had a pulse length of 6 ns, and the divergence of the beam was 26 mrad (86.5% energy content) as determined by a central fraction method (energy through an aperture) in the far field. The pulse energy was monitored by a calorimeter (Sciencetech MA10, Boulder, CO) and was varied from zero to a maximum of 3.5 mJ, by changing the power to the Nd:YAG flash lamps. A nitrogen UV laser (Laser Science Inc., Newton, MA) operating at 337 nm was used for some experiments.

The IR beam was focussed onto the probe tip using a 180 mm focal length  $\text{CaF}_2$  lens positioned outside a  $\text{CaF}_2$  viewport window. The diameter of the IR laser beam at the lens was 60 mm. The laser beam passed the window normal to the window surface and hit the sample at a  $60^\circ$  angle relative to the normal of the probe surface. The UV beam was focused onto the sample surface in an identical manner, except that the UV beam entered the ion source from the opposite side, through a silica lens and window.

There was a concern that low intensity laser light at  $1.57 \mu\text{m}$  and  $1.064 \mu\text{m}$ , leaking through the dichroic mirror in the IR laser path, might contribute to the desorption process. In control experiments, a Ge-plate that absorbs at both of these wavelengths, but transmits efficiently at  $3.28 \mu\text{m}$ , was inserted into the beam path. No differences in the mass spectra were observed, with or without the Ge-filter, when compared at the same pulse energy.

The focal spot size on the probe tip was measured by the following procedure. When the probe tip was covered with a fine graphite powder, the luminescence of the irradiated area was easy to distinguish on the TV monitor. The focal spot was seen to be ellipsoidal and, by comparing with the known dimensions of the probe tip, it was determined that the irradiated surface area was  $0.5 \text{ mm}^2$ . Correcting for the  $60^\circ$  incidence angle, the laser beam cross section is found to be  $0.25 \text{ mm}^2$ . With a typical pulse energy of 3.0 mJ, and correcting for 10% Fresnel losses in the lens and 10% reflection losses in the chamber window, the energy fluence (perpendicular to the laser beam),  $I_0$ , is calculated to be  $1.0 \text{ J/cm}^2$  and the irradiance  $1.9 \times 10^8 \text{ W/cm}^2$  at the focal point. The energy deposition in the sample closest to the surface (at a depth that is small relative to  $1/\epsilon$ , where  $\epsilon$  is the absorption coefficient) is  $\epsilon \times I_0$ , where

$I_0$  is the energy fluence in the laser pulse. The absorption coefficient for water ice at  $3.28 \mu\text{m}$  is approximately  $2.5 \times 10^3 \text{ cm}^{-1}$  [9]. For frozen glycerol, we have measured an absorption coefficient of  $1.5 \times 10^3 \text{ cm}^{-1}$ . Assuming an actual absorption coefficient in our samples is  $2 \times 10^3 \text{ cm}^{-1}$ , we find that energy is deposited in the outermost surface layer with a density of  $2 \times 10^3 \text{ J/cm}^3$ . The energy absorbed may be further lowered by reflection losses in the sample surface and by a decrease in the water absorption coefficient, at  $3.28 \mu\text{m}$ , during irradiation [22].

The liquid solvent consisted of water and glycerol (33:67 w/w), unless otherwise noted. This is the eutectic composition of water and glycerol, and the mixture is thermodynamically stable as a liquid to  $-46^\circ\text{C}$  [36]. Proteins or peptide analytes were dissolved directly into the solvent at room temperature at concentrations from  $0.5 \mu\text{M}$  to  $1 \text{ mM}$ . The sample probe tip was cleaned with ethanol, and about four microliters of analyte solution in glycerol/water were typically deposited on the probe surface. A small amount of solid powder was placed on the liquid surface using a spatula, and after a few seconds, any excess dry powder was blown off the sample. Some solid powders like nicotinic acid had good wetting properties and quickly formed evenly distributed suspensions. Other powders with poor wetting properties, like polystyrene, tended to remain on the liquid surface. In those cases, suspensions were formed on the probe tip by stirring the powder into the solvent with a spatula for up to one minute. Sufficient powder was added to give the suspension a slurry-like appearance. After stirring, the surface of the slurry was seen to gradually become smooth, but this process was relatively slow. If too much solid powder was added, the

fluidity of the suspension was lost, and inferior mass spectra were obtained. If too little powder was added, reproducibility suffered and ion intensities decreased. For nicotinic acid, between 0.3 mg and 0.5 mg powder was added per 1  $\mu\text{L}$  solvent. All chemicals used in this work were obtained commercially.

Samples of bacteriorhodopsin were prepared by adding 4  $\mu\text{L}$  of 2-pentanol to 4  $\mu\text{L}$  of a suspension of purple membranes in the glycerol/water solvent. The nicotinic acid crystals were then added, and the suspension was observed to turn yellow. The yellow color indicated that the protein partially denatured in the presence of the nicotinic acid crystals, possibly because the pH decreased to 3.5.

After preparing a suspension, the probe tip was cooled by immersion into liquid nitrogen. With the eutectic glycerol/water mixture, this cooling resulted in the formation of a vitreous phase, with essentially no ice crystal formation [37]. Immersion of the sample into liquid propane resulted in much faster cooling, but did not change the mass spectra when the glycerol/water eutectic mixture was used. A thin water frost layer was formed on the cold sample surface as the probe was transferred from the Dewar, where it was frozen, to the vacuum lock of the mass spectrometer. Using a 1 Hz laser repetition rate to obtain single shot mass spectra on the oscilloscope, it was found that weak protein ion peaks were observed from the first laser shots. The protein peaks gradually approached their full intensity during the first 50 laser shots at 3 mJ.

To avoid the formation of a frost layer, the room temperature probe tip with the eutectic glycerol/water sample solution could be inserted into the ion source. The sample was

then cooled *in situ* upon contact with the pre-cooled sample electrode. The cooling was still fast enough (about 1 minute to reach  $-130^{\circ}\text{C}$ ) that the eutectic solution formed a vitreous phase [37]. The protein mass spectra obtained with in-situ cooling were indistinguishable from the ones obtained by fast cooling in liquid nitrogen (after ablation of the frost layer). However, all spectra shown in this paper were obtained by immersion of the sample in liquid nitrogen. Cooling below  $-100^{\circ}\text{C}$  did not significantly change the mass spectra. All spectra were obtained at  $-140\pm 5^{\circ}\text{C}$ , unless otherwise noted.

About half of the compounds tested in this work as cryo-IR-SALDI solids had a low or negligible solubility in glycerol/water. However, other solids used, such as nicotinic acid and the amino acids, had a significant solubility. If all the added crystals dissolved fully, no mass spectra were obtained from the bulk of the frozen solutions. Some solids, in particular aspartic acid and histidine, dissolved quickly. Additional powder typically had to be added to ensure that some crystals remained. The dissolution of the soluble solids could be arrested by quickly freezing the sample. Essentially no additional dissolution was observed once the suspensions had been cooled to below  $-40^{\circ}\text{C}$ . However, fast freezing also tended to result in an uneven distribution of solid particles in the suspension, and this made it more difficult to obtain high quality mass spectra. A better alternative was to slow the rate of dissolution by pre-cooling the probe and the liquid sample solution to about  $0^{\circ}\text{C}$  prior to adding the soluble powder. There was then enough time to distribute the solid evenly throughout the suspension.

Control experiments were performed in which either the organic solid or the glycerol was eliminated from the sample. In the absence of organic solids, mass spectra (of peptides) were only occasionally obtained from the bulk of the frozen phase, and these rare events may well have been due to contamination of the sample by solid particles. In experiments where the glycerol cryoprotectant was not present, it was necessary to freeze the sample prior to inserting the probe into the ion source because the high vapor pressure of water near room temperature led to severe loss of the water solvent in the vacuum. Mass spectra were obtained in the absence of glycerol, as described in the Results and Discussion section.

It is well known that laser desorption mass spectra can be obtained from metal surfaces [8,25,28]. For this work, it was necessary to verify that the mass spectra were obtained from the bulk of the frozen suspensions without involvement of the underlying metal surface. "Laser drilling" experiments were performed where 4  $\mu\text{L}$  of the glycerol/water nicotinic acid suspension was first deposited on the probe, and series of laser pulses were delivered to the same spot close to the center of the sample where the sample thickness was approximately 0.30 mm. The copper surface was reached after about 2,500 laser pulses (about 4 minutes at 10 Hz) with a 3 mJ laser pulse energy. That the copper surface was indeed reached at this point was clearly revealed by bursts of intense ion signals due to  $\text{Na}^+$ ,  $\text{K}^+$ , and  $\text{Cu}^+$  that were not seen from the bulk suspension. Thus, the ablation yield was approximately 0.1  $\mu\text{m}$  per 3.0 mJ laser pulse, and the volume of frozen solution desorbed per laser shot was less than 0.1 nL. Unless otherwise noted, the sample size used in this work was 4  $\mu\text{L}$ , the laser was focussed close to the center of the frozen sample, and all spectra

reported were obtained prior to 2 minutes irradiation time (at each spot) at 10 Hz. Under these conditions, the maximum depth of ablation should be less than 25% of the sample thickness.

### Results and Discussion

The goal of this work was to obtain mass spectra of biomolecules directly from bulk frozen aqueous solutions. In initial experiments, no solid crystals were added to the analyte solutions in glycerol/water. It was found that the Nd:YAG/OPO laser beam at 3.28  $\mu\text{m}$  was efficiently absorbed by frozen water and glycerol/water solutions, and sample drilling experiments showed that the ablation yield was about 0.3  $\mu\text{m}$  per 3 mJ laser shot [38]. However, we had little success in obtaining mass spectra from the bulk of frozen water or glycerol/water solutions, although peptide mass spectra were occasionally obtained [38]. This is in general agreement with results of Williams et al. [26,27,39] and Hillenkamp et al. [8].

Because useful analyte mass spectra were not obtained from bulk, frozen aqueous solutions, we explored the use of Surface-Assisted Laser Desorption Ionization (SALDI) mass spectrometry [33] to obtain spectra from frozen water solutions. Suspensions of graphite (or activated carbon) particles in aqueous solutions were frozen and irradiated with the 3.28  $\mu\text{m}$  Nd:YAG/OPO laser. It was found that mass spectra of organic molecules and peptides were easily and reliably obtained [34]; however, we were not successful in obtaining mass spectra of proteins larger than myoglobin. In an effort to overcome this limitation, we

explored the use of organic crystals, instead of carbon powder, for cryo-IR-SALDI in frozen, aqueous solutions.

### Cryo-IR-SALDI mass spectra of peptides

We first present typical cryo-IR-SALDI results for peptides, before discussing results for proteins. For the mass spectrum of angiotensin II in Figure 1, a suspension of nicotinic acid crystals was prepared and frozen as described in the Experimental section. It is seen that the mass spectrum is dominated by the protonated peptide peak at  $m/z=1047$  and by peaks due to the SALDI solid. Low-intensity clusters of glycerol with  $\text{Na}^+$  and  $\text{K}^+$  are also sometimes observed.

The mass resolution, ( $m/\Delta m$ , FWHM), for the peptide peak in Figure 1 is approximately 80. The intensity of the angiotensin peak is low relative to the matrix peaks in the spectrum in Figure 1. This spectrum was obtained at a 1.25 mJ laser pulse energy, and the intensity of the peptide peak was found to increase by about a factor of 10 when the laser pulse energy was increased to the maximum of 3.5 mJ. However, the mass resolution decreased somewhat at higher laser pulse energies. By decreasing the pulse energy below 1 mJ, a mass resolution of 250 (FWHM) could be achieved. This is similar to the mass resolution obtained with UV-MALDI on the same instrument. Using the maximum laser pulse energy, the detection limit ( $S/N = 3$ ) for angiotensin II was approximately  $0.5 \mu\text{M}$ , or 0.5 pmole for a  $1 \mu\text{L}$  sample.

A 0.5  $\mu\text{M}$  detection limit corresponds to 0.5 pmole of peptide in a 1  $\mu\text{L}$  sample size. However, it is easy to use smaller sample sizes. In room temperature, activated carbon-UV-SALDI, we found that the minimum amount of analyte required was lowered by more than two orders of magnitude by introducing a solvent concentration step on the probe (similar to solvent evaporation in MALDI) and by using smaller sample sizes. These strategies should be possible to use also in cryo-IR-SALDI. The peptide sample consumption during the 100 laser shots used for the spectrum in Figure 2 was about 10 pmole. However, single shot mass spectra were obtained with a peptide consumption of approximately 1 fmole.

Figure 2 shows the abundance of protonated nicotinic acid and protonated angiotensin II, as a function of laser pulse energy in a double logarithmic plot. As the laser pulse energy is increased, the ratio of the abundances of these two ions remains nearly constant up to 1.5 mJ pulse energy, after which the peptide ion abundance is seen to level off more quickly than that of protonated nicotinic acid. The slope of the straight lines at lower laser pulse energy in Figure 2 is approximately 9 for both the nicotinic acid and the peptide which shows that the ion yields increase as the 9th power of the laser pulse energy. This is similar to the slope observed for matrix ions in MALDI [40]. The amount of nicotinic acid in the sample used for Figure 2 was approximately 3,600 times the amount of the peptide, whereas the signal abundance ratio is seen to be about 20. Thus, the relative response for the peptide is much higher than for the SALDI solid.

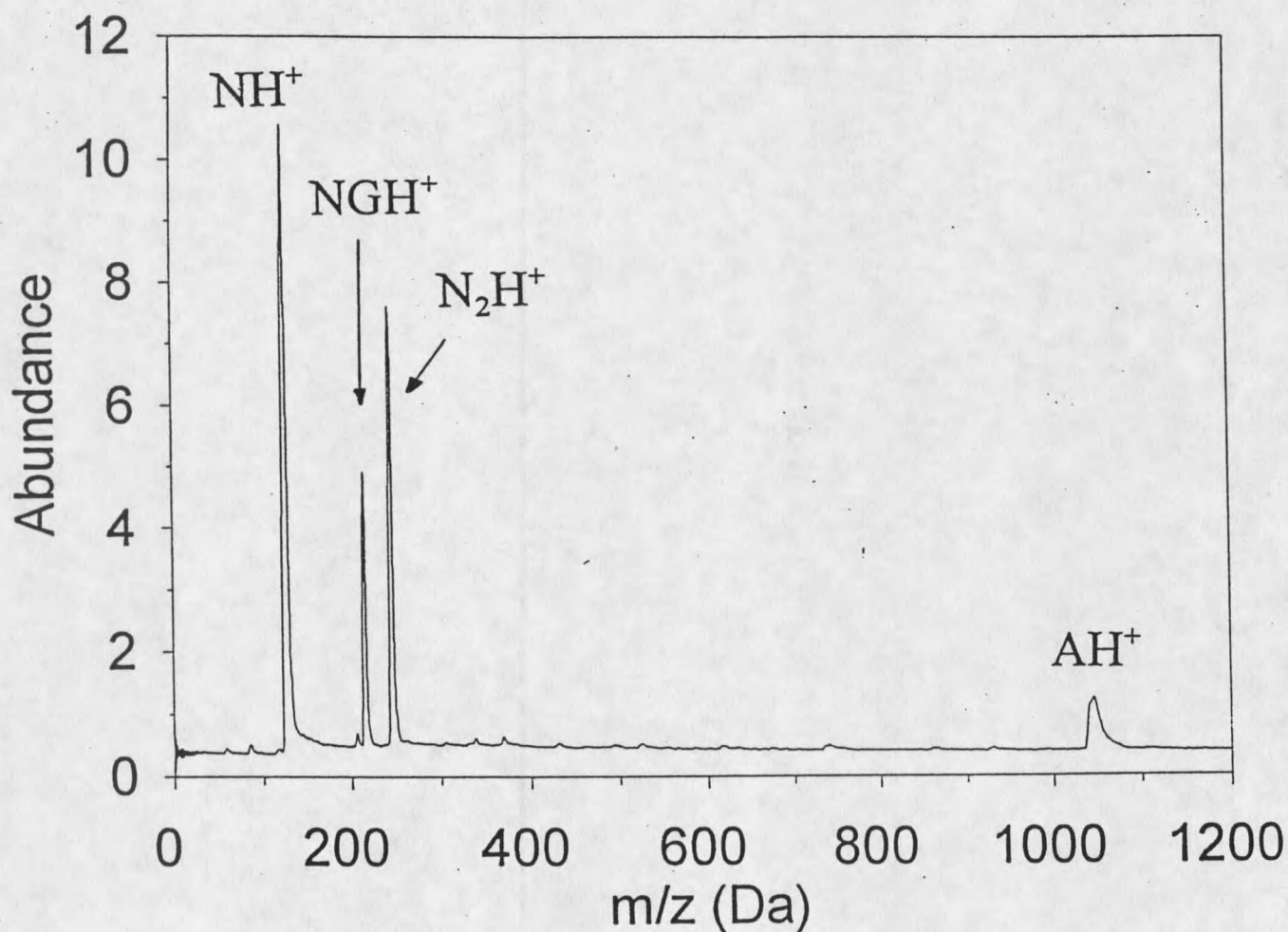


Figure 1. Cryo-IR-SALDI mass spectrum of 0.9 mM angiotensin II in 67% glycerol in water. Nicotinic acid (1.6 mg) was added to 4  $\mu\text{L}$  of the glycerol/ water solution before freezing by immersion of the copper sample tip in liquid nitrogen. Laser pulse energy 1.25 mJ, average of 100 single shot spectra, and low mass gate off. "N" = nicotinic acid, "A" = angiotensin II, and "G" = glycerol.

Comparison between different SALDI solids for protein desorption

We evaluated 20 different organic compounds as SALDI solids using a 0.5 mM equimolar mixture of myoglobin and cytochrome c in the eutectic glycerol/water solution, and the results are summarized in Table 1. Starting at the top of Table 1, the solids evaluated are ordered from the “best” to the “worst” SALDI solids. The approximate signal intensities for the protein peaks are given in the Table, as well as comments on sample preparation. With practice, protein mass spectra were obtained with 16 of the 20 solids. We were unsuccessful with only four of the compounds tested: sodium chloride, cellulose, carboxy-methyl cellulose, and tryptophan. Figure 3 shows a selection of cryo-IR-SALDI protein mass spectra, obtained using (a) nicotinic acid, (b) histidine, © xanthine, and (d) polystyrene as the SALDI solids. The spectra illustrate similarities and differences observed among cryo-IR-SALDI mass spectra using different solids. Singly and multiply charged protein peaks dominate the mass spectra. Several protein/heme and protein/protein clusters, with masses up to 50,000 Da, are resolved in the nicotinic acid and histidine-assisted mass spectra. The extent of multiple charging, and of clustering, is seen to vary between the SALDI solids.

The majority of SALDI solids tested were aromatic compounds, see Table 1. Aromaticity may well contribute to a compound being a successful SALDI solid, but it is not an absolute requirement. For example, aspartic acid crystals gave cryo-IR-SALDI mass spectra of myoglobin and cytochrome c, though the spectra were of lower quality (results not shown). Also, SALDI solids do not have to be volatile or have a low molecular

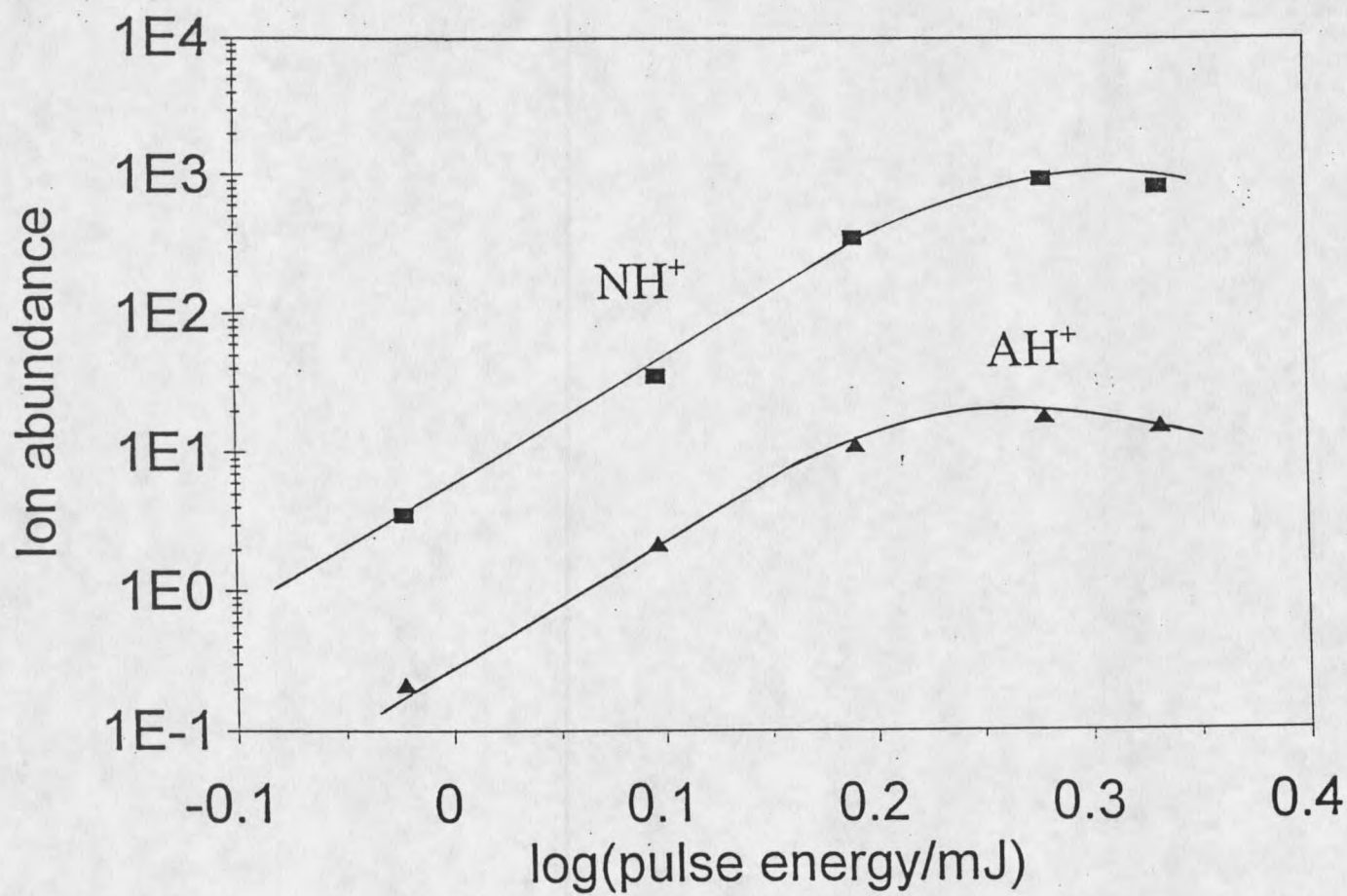


Figure 2 Abundances, as determined by peak heights, of singly protonated nicotinic acid (NH<sup>+</sup>) and singly protonated angiotensin II (AH<sup>+</sup>) ions as a function of laser pulse energy using the same experimental conditions as in Figure 1.

weight, as illustrated by the fact that polystyrene gave cryo-IR-SALDI mass spectra of proteins, Figure 3d.

The best protein mass spectra with respect to sensitivity and mass resolution were obtained with nicotinic acid, indole-2-carboxylic acid, thymine, and histidine. The mass resolution,  $m/\Delta m$  (FWHM), of the singly charged protein peaks at 15-20 kDa was typically about 50, with somewhat higher resolution obtained at the lowest laser pulse energies. The limit of detection for myoglobin and cytochrome c was about 5-10  $\mu\text{M}$ , compared to about 0.5  $\mu\text{M}$  for peptides, at a signal-to-noise ratio of three. The higher detection limit for proteins as compared to peptides is mainly due to the wider mass peaks for proteins. When peak areas in mass spectra (plotted versus flight time) were compared, it was found that the response for the proteins was close to that for the peptides.

Nicotinic acid was the SALDI solid of choice in this work. Mass resolution and sensitivity were as good as, or better than, those obtained with any of the other solids evaluated. Nicotinic acid, together with indole-2-carboxylic acid, was unique in that it reliably yielded protein mass spectra anywhere on the sample and with every laser shot. In addition, the nicotinic acid powder wets easily, and the suspensions were easy and quick to prepare.

#### UV-laser irradiation of cryo-SALDI samples

All solids in Table 1 were also tested for their ability to yield cryo-SALDI mass spectra with the 337 nm nitrogen UV laser. In most cases, no ions were observed when the UV laser was first focussed onto a freshly frozen SALDI suspension, but weak signals due

Table 1. Summary of cryo-IR-SALDI results for selected solids additives.

<u>Compound</u>	<u>Protein Mass Spectra Typical Intensity*</u>	<u>Comments</u>
nicotinic acid	5	wets well, fine uniform crystalline powder, rather soluble, low protein charge states
indole-2-carboxylic acid	5	wets well, insoluble, high protein charge, lower mass resolution than nicotinic acid
histidine	4	wets well, very soluble, reliability of analyte signal improved by pre-cooling the glycerol/water solvent before adding crystals
thymine	3-4	poor wetting, required stirring, slightly soluble, dendritic crystals, produces high protein charge states
alpha cyano-4-hydroxy cinnamic acid	2	wets well, almost insoluble, produces high protein charge states
pyrene	1	insoluble, large crystals
6-dimethylaminopurine	1	wets well, slightly soluble
guanine	1	wets well, almost insoluble
xanthine	1	wets well, slightly soluble, tendency to produce high protein charge states
adenine	1	wets well, slightly soluble
2,3-dihydroxybenzoic acid	1	poor wetting, required stirring
sinapinic acid	1	poor wetting, required stirring, insoluble
polystyrene powder (typical m.w. 4,000)	0.5	polystyrene powder was ground by mortar and pestle to remove trapped air, insoluble, required extensive stirring
terephthalic acid	0.5	extensive stirring required, fine powder, insoluble
diphenylamine	0.5	extensive stirring required, large planar crystals do not wet, insoluble
aspartic acid	.5	wets well, very soluble, reliability of analyte signals improved by pre-cooling the glycerol/water solvent before adding crystals
tryptophan	none	slightly soluble
sodium chloride	none	very soluble
cellulose	none	19 $\mu$ m particle size, wets well, insoluble
carboxy-methyl cellulose	none	insoluble, wets well

\*All 20 compounds were tested with a solution of 0.5 mM cytochrome C and 0.5 mM myoglobin in 67% glycerol in water, at -3.0 mJ per laser shot. Other conditions were as described in the Experimental section. Typical intensities represent the average of one hundred spectra and are quoted in arbitrary units.

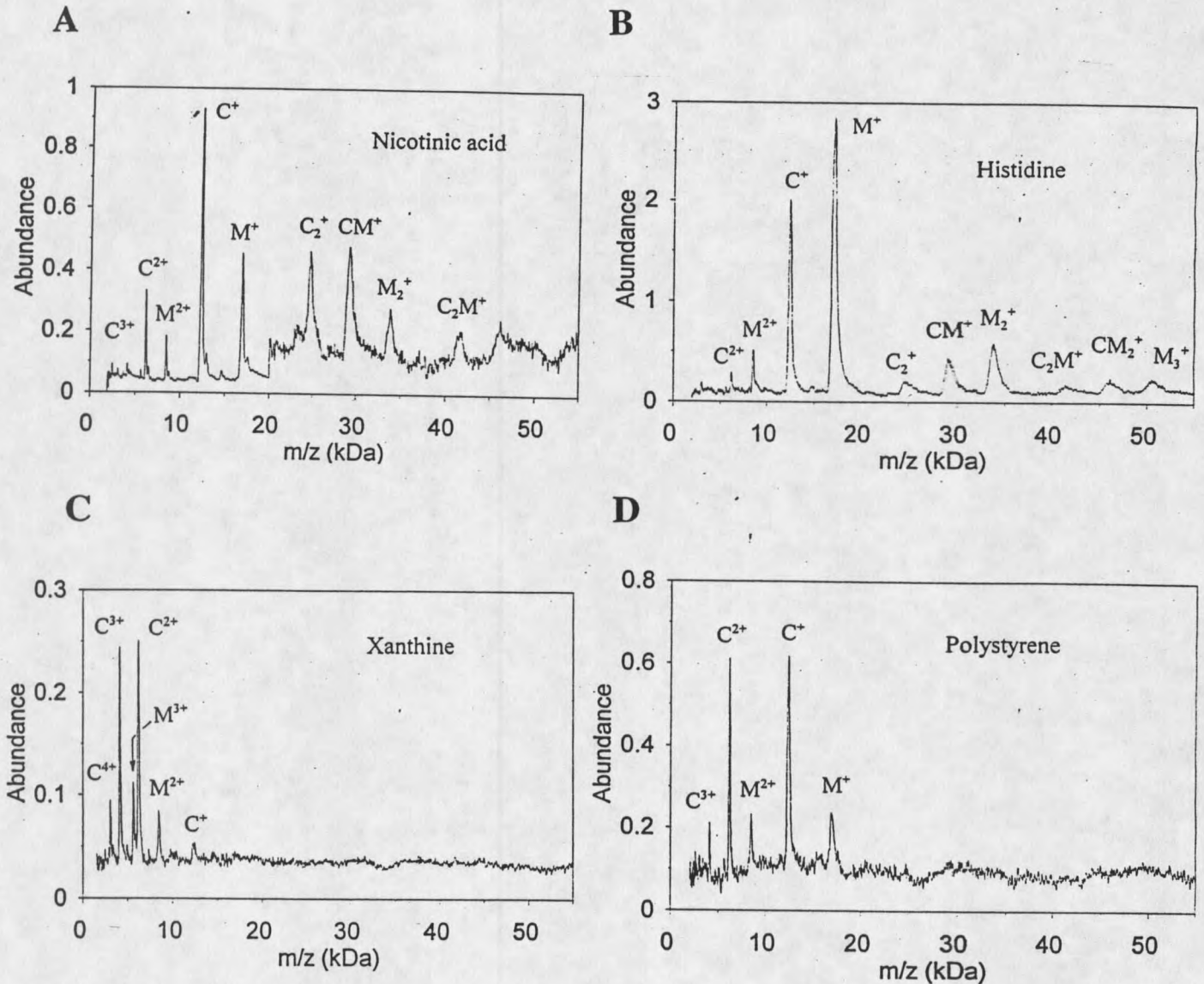


Figure 3 Cryo-IR-SALDI mass spectra of an equimolar mixture of 0.5 mM myoglobin ("M") and cytochrome c ("C") in a 67% glycerol in water solution with different SALDI solids added. a) Nicotinic acid, b) histidine, c) xanthine, and d) polystyrene. Each spectrum is an average of 100 single-shot spectra, and the laser pulse energy was 3.0 mJ.

to ions from the SALDI solid appeared after a few hundred laser shots. For a few solids with unusually large crystals, such as pyrene, as well as for suspensions with a concentration of solid that was high enough that the fluidity of the sample was lost prior to freezing, abundant ions from the SALDI solid were observed from the beginning of UV irradiation. In these samples, it seems likely that crystals protruded out of the sample surface. In additional experiments, samples were first exposed to about 200 IR laser shots of 3 mJ each, during which time protein mass spectra were observed. The shallow "crater" that resulted from the IR laser ablation could be clearly seen on the TV monitor. When the nitrogen UV laser was focussed onto this area, ions from the SALDI solid were observed from the first UV laser shot. These results indicate that the organic crystals must be exposed on the surface of the sample in order to obtain ions from cryo-SALDI samples with the UV laser. Peptide mass peaks were observed in the UV-induced spectra from the cryo-SALDI samples, but only for one solid (indole-2-carboxylic acid) was a (very weak) protein peak obtained and then only at maximum UV laser power.

#### Laser "drilling" experiments and surface charging

Insights into the analytical potential of cryo-IR-SALDI, and into the mechanisms of ion formation, were obtained from laser "drilling" experiments on nicotinic acid and thymine suspensions in frozen glycerol/water. In these experiments, the IR laser was focussed onto the same sample spot for an extended time. As described in the Experimental section, the copper substrate was reached after about 2,500 laser shots with 3 mJ of 3.28  $\mu\text{m}$  laser energy

in each pulse when a 4  $\mu\text{L}$  sample was used. Protein ion signals were obtained during the entire drilling time. (Remarkably, protein ion signals were obtained from the bottom of the drilled crater for more than 30,000 laser shots. These results, that required the presence of the organic crystals on the metal surface, will be published elsewhere).

During the drilling process, it was observed that the flight time for the ions drifted significantly. For example, with an acceleration voltage of 20,000 V, the flight time for singly charged apomyoglobin ions (16,953 Da) was 95 to 98  $\mu\text{s}$  at the beginning of drilling. The flight time gradually decreased during drilling and was 93  $\mu\text{s}$  as the metal surface was reached. The flight time calculated from the known length of the flight tube was also close to 93  $\mu\text{s}$ . The longer ion flight times observed from the surface of a frozen sample did not vary significantly with laser power. However, there was a correlation with the thickness of the sample - the thicker the original sample, the longer the initial flight time. These observations can not be explained by changes in desorption characteristics, such as a "drying" of the sample during drilling. We therefore concluded that the unexpectedly long initial flight times must be due to the sample surface being at potential lower than that of the metal. This implies that the frozen surface carried a negative charge. In our experiments, the potential of the copper probe was 20 kV. The observed flight times show that the potential of the surface of the frozen sample, at the onset of drilling, was in the range of 18 to 19 kV. It is of interest to note that the charge required to achieve this surface potential is only about 200 singly charged ions per  $(\mu\text{m})^2$ . With a sample thickness of 0.2 to 0.3 mm, the electric field strength in the frozen sample is found to be approximately  $5 \cdot 10^4$  V/cm. The upper limit for

the electric field strength may well be determined by the leakage of charge carriers between the metal surface and the sample surface.

It is not unreasonable that the sample surface would become negatively charged early in the laser irradiation since positive, but not negative, ions leave the surface during the desorption process. It is also possible that the ionization gauge, or low-current discharges along insulator surfaces in the high-voltage source, supplies the gas-phase ions required to charge the frozen sample surface.

#### Larger proteins and clustering

Mass spectra of small proteins, such as myoglobin and cytochrome *c*, are sometimes obtained with methods that will not yield spectra of larger proteins. Room temperature carbon-UV-SALDI, for example, was found to have an upper mass limit of about 20,000 Da [33]. Thus, the question of what size range of proteins can be studied using cryo-IR-SALDI is of considerable interest. Figure 4 shows a nicotinic acid-SALDI mass spectrum obtained from a solution containing lactic dehydrogenase (LDH, 0.05 mM) and cytochrome C (at 0.10 mM). LDH is a tetrameric protein with four identical subunits and a total molecular weight of 146,256 Da. The highest-intensity peak in Figure 4 is that of the LDH monomer, but complexes containing 2, 3, and 4 subunits are also seen. The question arises whether the multimeric complexes could be "surviving" fragments of the intact LDH protein and thus reflect specific subunit associations. However, the gradual decrease in the intensity of the LDH subunit complexes with increasing size and the presence of several low-intensity peaks

that are due to mixed complexes between LDH subunits and cytochrome C make it more likely that non-specific clustering occurred. Other systems likewise showed extensive molecular complex formation. For example, series of peaks in nicotinic acid-SALDI mass spectra of a mixture of 0.5 mM lysozyme (m.w. 14,300 Da) and 1.1 mM angiotensin in glycerol/water were due to clusters with up to five lysozyme and several angiotensin molecules (results not shown). Proteins larger than the LDH subunit can be analyzed by cryo-IR-SALDI. The nicotinic acid-SALDI mass spectrum of bovine serum albumin (BSA) in Figure 5 shows an intense molecular ion mass peak with a mass resolution of about 50. Smaller peaks are due to doubly charged BSA and to singly and triply charged BSA dimers. The weak peak at  $m/z=99.6$  kDa is due to a doubly charged BSA trimer (199 kDa).

For some protein samples, we have observed very broad peaks due to unresolved distributions of complexes or clusters. For example, in experiments where SDS was added to an aqueous solution of lysozyme, a very broad, nearly symmetric peak was observed (results not shown). The apex of the peak corresponded to about four SDS molecules per lysozyme molecule. Dissociation of SDS-protein complexes in the ion acceleration region would explain why peaks due to the protein with different numbers of SDS molecules were not resolved. This result is in sharp contrast to room temperature graphite-SALDI where peaks due to protein molecules, without SDS, were obtained even when 5 to 10 % SDS had been added to the sample. In another series of experiments in this work, cryo-IR-SALDI mass spectra of the integral membrane protein bacteriorhodopsin were obtained directly from a suspension of purple membrane from *Halobacterium Salarium* in glycerol/water. Native

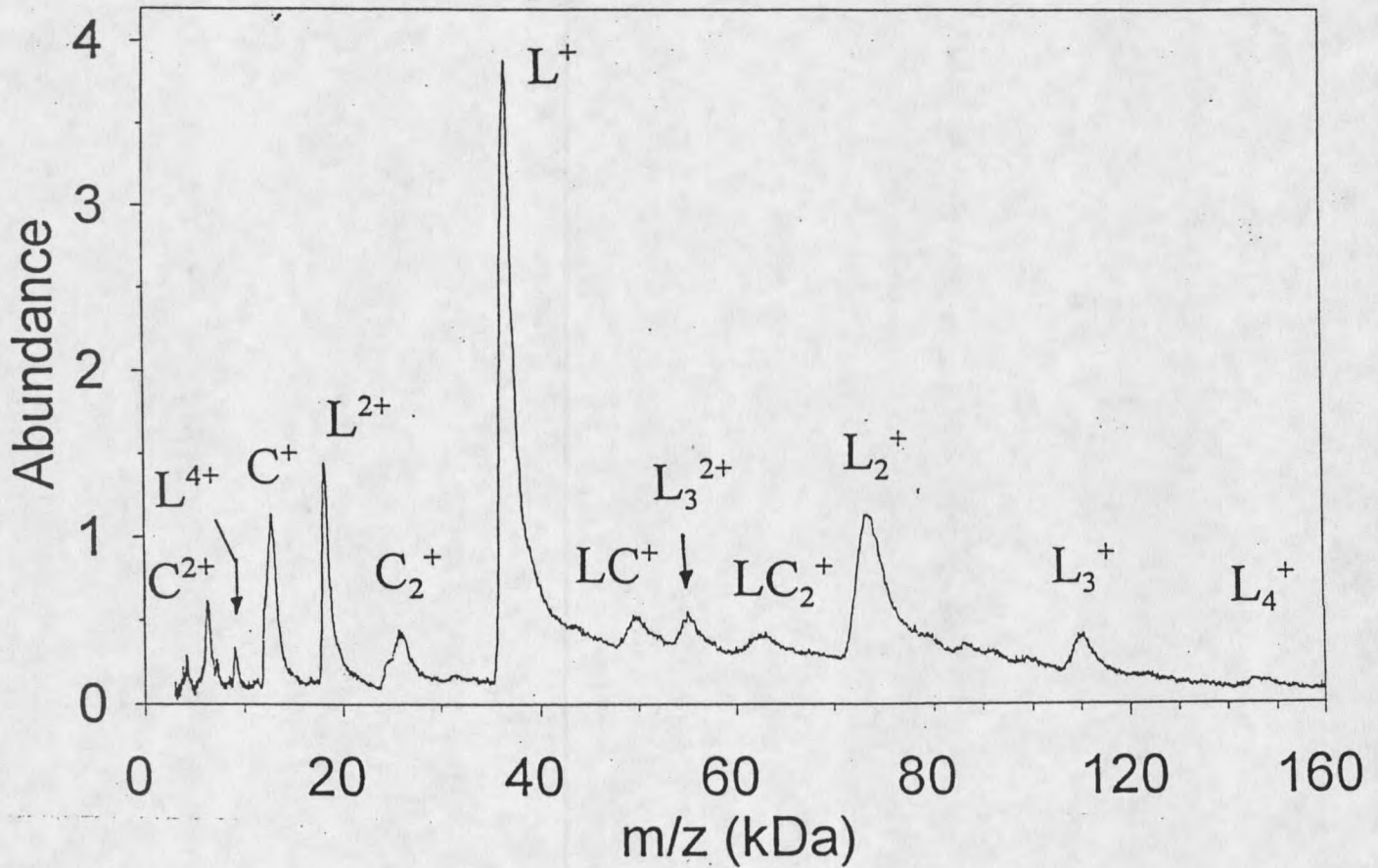


Figure 4

Nicotinic acid cryo-IR-SALDI mass spectrum of 0.05 mM lactic dehydrogenase ("L") and 0.10 mM cytochrome c ("C") in water:ethanol:glycerol (25:25:50, v:v:v). The average of 100 single shot spectra is shown. Essentially the same spectrum was obtained in the absence of ethanol. Note change in mass scale at 80 kDa.

purple membranes contain a high concentration of bacteriorhodopsin embedded in a lipid bilayer with about 11-13 lipids per bacteriorhodopsin dimer. In the mass spectra (not shown), the protein peak was observed to be very broad, and the width of the peak showed that individual bacteriorhodopsin molecules were associated with up to 12 lipid molecules. However, a distinct peak ( $m/\Delta m=65$ ) superimposed on the leading edge of the broad distribution allowed for accurate mass determination of the protein, free of any lipid. Clearly, cryo-IR-SALDI is able to desorb proteins from a wide range of physical environments, but it is not always possible to fully dissociate proteins from neighboring molecules using current approaches. There is a need to better understand the factors that determine internal energy deposition, such that the extent of cluster dissociation and the quality of the mass spectra can be optimized for different types of samples.

#### Results from aqueous solutions with no cryoprotectant added

In this work, we have mainly used the eutectic mixture of 67% glycerol in water as the SALDI solvent. As described in the Experimental section, this mixture forms a vitreous (amorphous) phase, even when using the relatively slow cooling method of immersion of the sample holder into liquid nitrogen [41]. The eutectic mixture was used because we initially believed that suppressing water ice crystal formation was essential. However, it was found that lower concentrations of the glycerol cryoprotectant could easily be used. Even with pure water solvent, the mass spectra were very similar to those obtained with 67% glycerol in

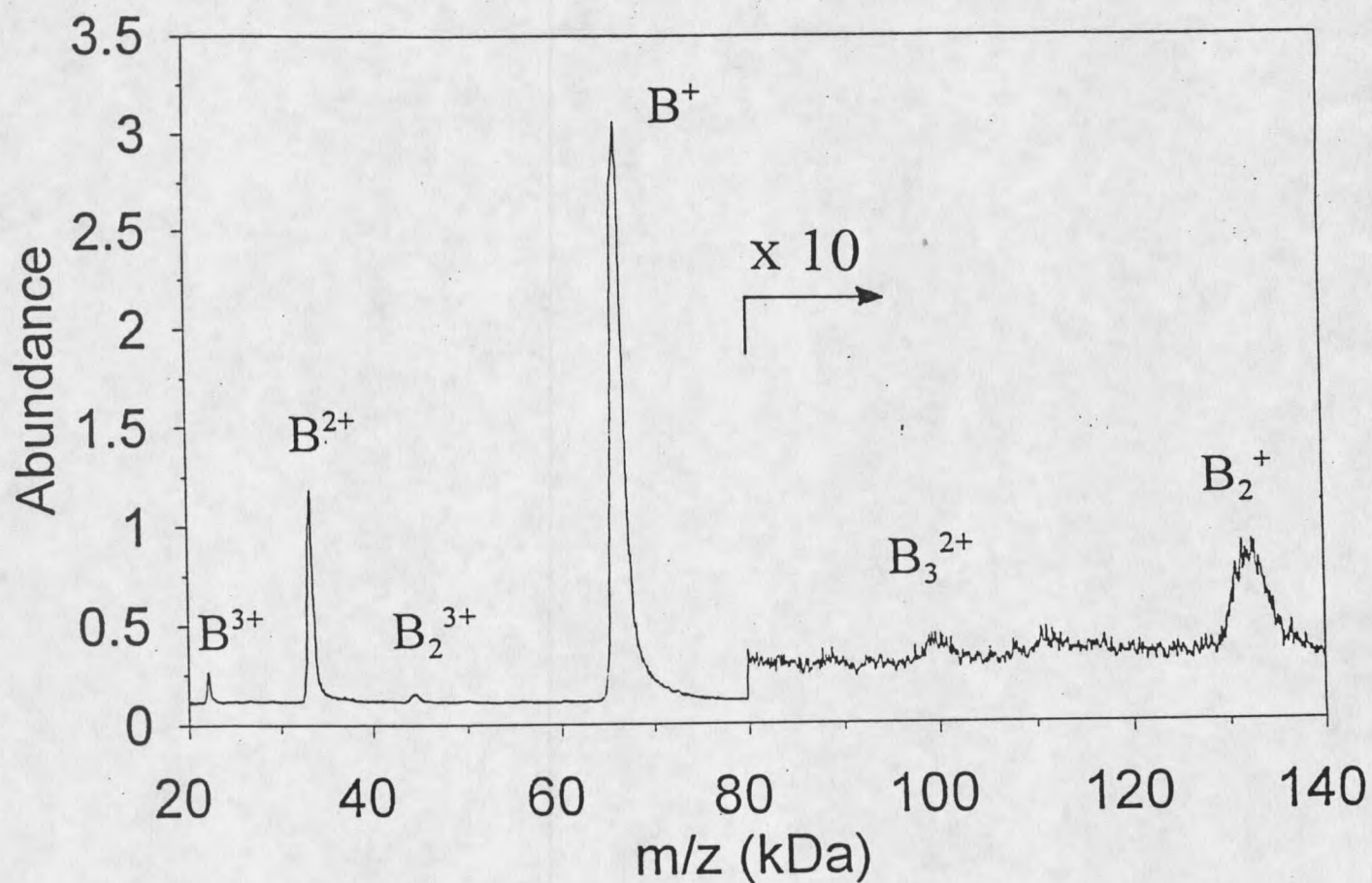


Figure 5 Nicotinic acid cryo-IR-SALDI mass spectrum of 0.34 mM bovine serum albumin ("B", 66,430 Da) in glycerol/water; average of 100 single-shot spectra.

water. Though not required, the addition of glycerol was very beneficial to suppress sweet-spot formation and to achieve a uniform sensitivity over the whole sample surface. When an aqueous sample is cooled in the absence of cryo-protectant, analytes concentrate in the void-volumes ("freeze concentrate") between the growing crystals of water ice [42]. The resulting concentrated solution of proteins or other analytes are, in effect, dried by the formation of pure water crystals. The water content in the protein concentrate can vary from a few to about 40 percent by weight [42]. The "freeze concentrate" would seem to be similar to the protein films, air-dried on metal surfaces, from which laser desorption mass spectra of proteins have previously been obtained [7,8,26,27]. It is possible that the desorption processes are similar, except that metal surfaces were involved in the previous work and solid organic surfaces are used in the present work.

### Multiple charging

Multiple charging of proteins is observed in most cryo-IR-SALDI mass spectra, as illustrated in Figures 3 and 4-6. It was found that the extent of multiple charging varied significantly between different SALDI solids but, for a given solid, the extent of multiple charging did not depend on the laser power. For the majority of SALDI solids tested, singly and doubly charged protein ions dominated the mass spectra. However, many solids yielded intense peaks corresponding to protein charge states of three to five, see for example Figure 3c. Of the twenty SALDI solids in Table 1, thymine,  $\alpha$ -cyano-4-hydroxy-cinnamic acid, indole-2-carboxylic acid, and xanthine yielded protein mass spectra with the highest charge

states. Figure 6 shows a thymine-SALDI mass spectrum of myoglobin with a charge distribution from  $MH^+$  to  $MH_{12}^{12+}$ . The solution had been acidified to pH 4 by adding HCl. The charge distribution shifted from a maximum of 8 charges without acid addition to 12 charges with added acid.

High protein charge states have previously been reported in IR-MALDI. For example, a 150 kDa monoclonal antibody was observed with up to 13 charges [10]. In room temperature, carbon-SALDI, we have observed myoglobin with up to 6 charges. However, the high charge states observed here for a small 17 kDa protein seems unprecedented in laser desorption. Indeed, the high charge states in Figure 6 is approaching those observed for the native protein in electrospray, when using an aqueous solution [43], though even higher charge states, up to 23+, are observed in electrospray when the protein is denatured.

### *Ionization Processes*

Tentative conclusions can be made regarding the ionization processes in cryo-IR-SALDI. Since the SALDI solid is essential in order to produce gas-phase ions, it might seem reasonable to assume that the high-abundance "SALDI solid ions" (i.e. ions originating from the SALDI solid) are reagent ions that ionize neutral analyte molecules in ion/molecule reactions. However, this does not seem to be the case.

In considering the ionization processes in cryo-IR-SALDI, it is useful to compare with a better understood desorption ionization method such as FAB. In FAB, the analyte is homogeneously mixed with a matrix in a solution. Ionization transfer occurs from matrix ions

to neutral analyte molecules and, as a result, protonated matrix ions in FAB are significantly suppressed by the presence of only 1-2 mole percent of a higher proton affinity analyte [39]. In SALDI, the experimental observations are different: Between two analytes that are both present in the liquid phase in room-temperature graphite SALDI, ion suppression effects are significantly stronger than in FAB [33]. In contrast, we have found that suppression effects in cryo-IR-SALDI, between ions derived from the solid compound and ions derived from the frozen solution, are small. For example, when 20% of the high proton-affinity compound diethanolamine was added to the glycerol/water phase, in a suspension with nicotinic acid, it was found that the nicotinic acid ion signal was suppressed by only about 50%. This shows that most nicotinic acid ions experience few collision in the desorption plume with molecules from the frozen phase. Otherwise, few nicotinic acid ions would have survived proton transfer to diethanolamine. Thus, there is only limited mixing between the SALDI solid and the frozen phase, either in the sample or in the desorption plume.

There is good evidence that analyte ions in cryo-IR-SALDI are preformed, i.e. already present in the frozen phase prior to the desorption event. First, the only possible reagent ions present in the mass spectra are the ions derived from the SALDI solid. Because of limited mixing with molecules from the frozen phase, as explained above, it seems unlikely that these are reagent ions. Second, in comparing IR- and UV-induced cryo-IR-SALDI mass spectra, large variations were observed for the abundances of the SALDI solid ions. For example, nicotinic acid ion abundances were two to three orders of magnitude higher with the IR than with the UV laser, whereas the abundances of indole-2-carboxylic acid ions were a factor of

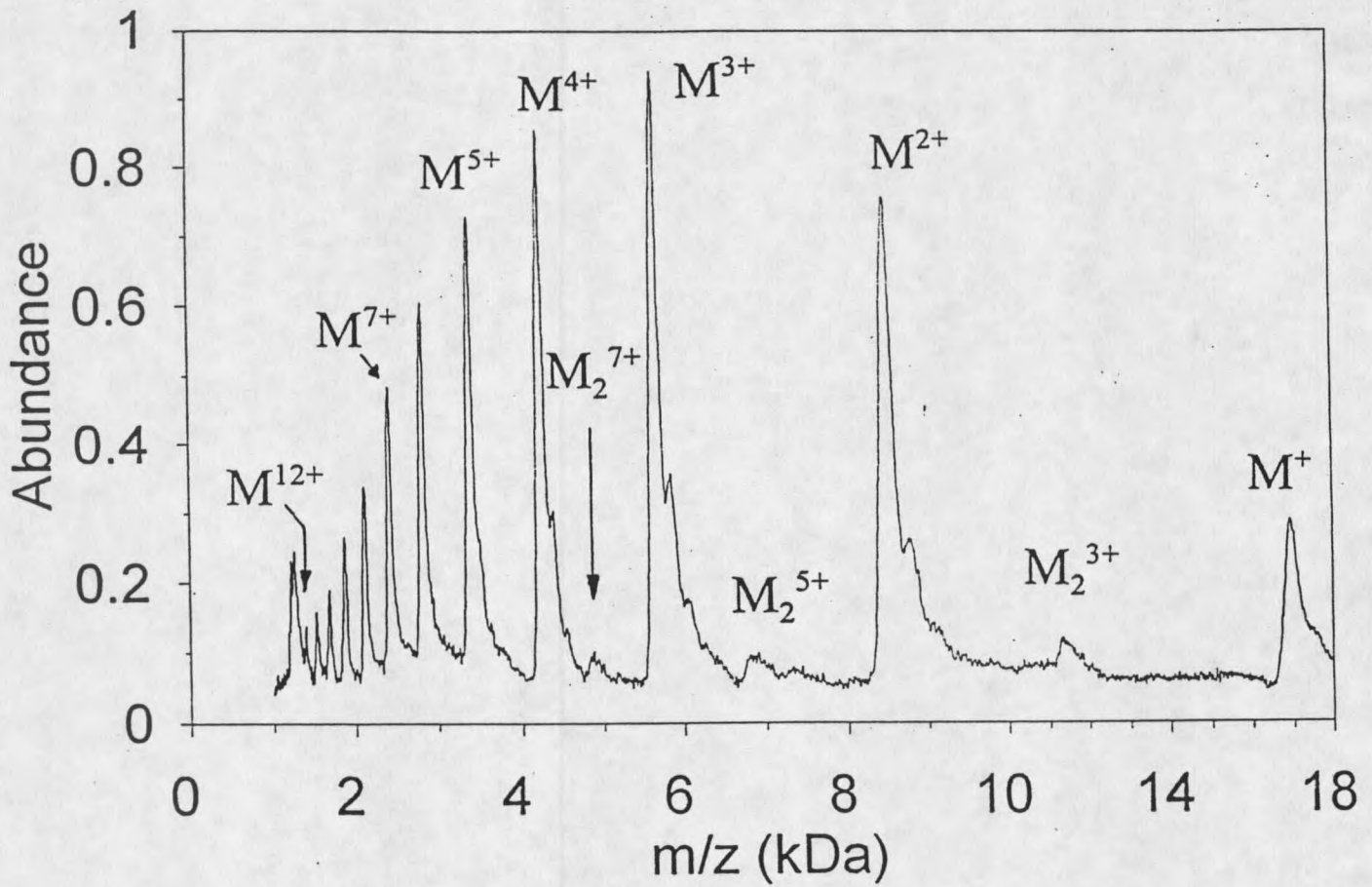


Figure 6

Thymine cryo-IR-SALDI mass spectrum of 0.1 mM myoglobin ("M") in 67% glycerol in water; HCl was added to give a pH of 3.5 in the final suspension. Average of 100 spectra. Note change in mass scale at 10 kDa.

2-3 higher with the UV laser. These large intensity variations were not reflected in the abundances of analyte and glycerol ions, as would have been expected had the SALDI solid ions been the precursors of the ions from the frozen phase. Third, the most convincing evidence for analyte ions being preformed in cryo-IR-SALDI comes from the observation of extensive multiple charging of protein ions. It is extremely difficult to form ions in charge states higher than one by gas-phase ion-molecule reactions because of the strong electrostatic repulsion between a singly charged ion and a reagent ion of the same charge. Thus, multiply protonated ions must have been present in the condensed phase prior to the laser pulse (i.e. "preformed").

The discussion above leads to a picture of the cryo-IR-SALDI desorption ionization process where 1) ions originate **both** from the SALDI solid phase and from the frozen phase; 2) there is limited mixing, in the sample and in the desorption plume, between the molecules of these two phases; and 3) most analyte ions are **preformed**.

The conclusion that analyte ions, observed in cryo-IR-SALDI mass spectra, are preformed in the frozen phase does not answer the question of why the SALDI solid is required to observe analyte ions. The crucial function of the solid may well be to facilitate charge separation. The observation of highly charged protein ions in cryo-IR-SALDI requires that the multiply charged ions, present in solution, be separated from their counter ions. To see why this represents a problem, we may consider the minimum distance by which a counterion must be separated from a charged protein, in order for the applied electric (extraction) field to overcome the electrostatic, attractive force between the ions. For the

8,000 V/cm ion extraction field, used in this work, and for a singly charged ion and a singly charged counter-ion, the required separation distance in vacuum is calculated to be 42 nm in the direction of the extraction field. This minimum distance increases approximately with the square root of the number of charges on the protein, and exceeds 100 nm for a protein with six charges. (In the dense plume, the dielectric constant is larger than one. However, the calculation of the minimum separation distance is only weakly dependent on the dielectric constant, since both ion/ion attractive forces and the extraction field are attenuated to nearly the same degree). Should more than one multiply charged protein be present nearby in space, the calculated minimum distances become larger, approaching 1  $\mu\text{m}$ . It is important to note that the calculated minimum separation distances are comparable to the thickness of the sample layer ablated per laser shot, 0.1 to 0.3  $\mu\text{m}$  [38]. This calculation shows that achieving charge separation in the laser-generated desorption plume must be expected to be a significant barrier to successful ion desorption, particularly for multiply charged ions. The problem of extracting positive ions from the frozen sample surface in the present cryo-IR-SALDI experiments seems even more daunting when it is considered that the surface carries a significant net charge of opposite sign (here negative), as concluded above. An attractive solution to this problem would be that the counter-ions are "immobilized", i.e. they would remain in that part of the sample that is not ejected into the vacuum. Minimum separation distances in the sample, prior to laser desorption, could then be significantly shorter because the expanding dense plume will exert a viscous force on the positive charges and this will facilitate charge separation.

One possibility for achieving charge separation in the sample is that the counter-charges are associated with the SALDI solid surfaces. To explore this possibility, we will consider thymine and  $\alpha$ -cyano-4-hydroxy-cinnamic acid. Exposed amino groups on thymine crystal surfaces are expected to be partially protonated at the low pH employed, giving the surfaces a net positive charge. In contrast, exposed carboxylic groups in  $\alpha$ -cyano-4-hydroxy-cinnamic acid should be partially deprotonated giving these surfaces a net negative charge. However, both these solids yielded cryo-IR-SALDI mass spectra with protein ions in high, positive charge states. Indeed, we have found no correlation between  $pK_a$ -values for the SALDI solids and their tendency to produce protein ions. Also, experiments using ion exchange chromatography beads as the SALDI solids were unsuccessful. For these reasons, we have tentatively concluded that crystal surface charging is not important to the formation of (multiply charged) analyte ions.

A second possible explanation for successful charge separation in the cryo-IR-SALDI sample is that the crystals might create local electric fields that are significantly higher than the 8,000 V/cm extraction field applied in our laser desorption ion source. Only charge separation needs to be accomplished because the desorption process considered here is induced by the laser pulse and not by the electric field. Therefore, the electric field strength required is lower than that experienced by ions desorbed in electrospray ( $\approx 10^9$  V/cm). Strong, local electric fields would be created by edges or needle-like structures in the surface of the frozen suspensions. Scanning electron photomicrographs were obtained of nicotinic acid,  $\alpha$ -cyano-4-hydroxy-cinnamic acid, and thymine. The micrographs of nicotinic acid (that

yields low charge state mass spectra) were dominated by rounded shapes, with smallest structural features having dimensions of about 1  $\mu\text{m}$ . The images of the thymine and  $\alpha$ -cyano-4-hydroxy-cinnamic acid samples, solids known to yield high charge state mass spectra, were very different. Both samples had surfaces with complicated morphology that included extensive structural features such as tips and edges with characteristic dimensions smaller than 100 nm.

To achieve charge separation in local, high electric fields in the SALDI sample surface, it is not sufficient that structural features are small. It is also required that a sharp edge or a fine tip of the solid is protruding out of the sample surface. We were not able to study frozen samples with the scanning electron microscope; however, it seems likely that such protrusions are formed on the surface of a frozen SALDI suspension as the aqueous phase between SALDI crystals is efficiently ablated by the IR laser. Charge separation would be achieved also on larger structures with characteristic radii of the order of 1  $\mu\text{m}$  or larger, such as those seen in nicotinic acid. However, the calculated charge density on a protruding tip varies inversely with the radius of the tip. The significance of the sharper structural features in the solid is then that the charge density that can be maintained is large enough to support multiply charged protein ions.

In cryo-IR-SALDI, singly charged analyte ions are likely to be produced by the same process as multiply charged analyte ions. The reason is that if singly charged analyte (protein) ions were formed by a different process, one should find two intensity maxima in the protein

charge distributions, one for singly charged ions and one for multiply charged ions. Instead, a single maximum was always observed, see for example Figure 6

The only conditions that altered the protein charge distribution was the elimination of water from the sample by drying, or simultaneous exposure of the laser beam to the frozen analyte and the copper substrate surface. If the protein is dried in a ACHA saturated aqueous solution (as is done in conventional MALDI), lower charge states are observed. When ACHA is used as a cyro-solid in protein aqueous suspension, high charge states are observed if the laser is focused on the bulk of the sample. If the laser is focused on the interface of the copper substrate and the same frozen ACHA protein suspension, a shift to lower charge state ions is observed.

Following the discussion above, we propose that the formation of singly as well as multiply charged analyte ions in cryo-IR-SALDI involves charge separation, prior to desorption, in high, local electric fields on the points or edges of the organic crystals, followed by IR-induced desorption of the preformed ions. Sharp tips on the SALDI solid may be required for observation of high charge states. The presence of water also seems required for the preservation of high charge states. In Cryo-IR SALDI, water may shield electron protein recombination in the plume during desorption.

Following the discussion above, we propose that the formation of singly as well as multiply charged analyte ions in cryo-IR-SALDI involves charge separation, prior to desorption, in high, local electric fields on the points or edges of the organic crystals, followed by IR-induced desorption of the preformed ions. These desorption conditions are reminiscent of those in laser-enhanced field desorption. Buttrill et al. [44] reported pulsed

laser desorption experiments using the Nd:YAG laser fundamental at 1.06  $\mu\text{m}$  and a time-of-flight mass spectrometer. However, mass spectra were obtained only of small ions [44].

As discussed in the Introduction, efforts to obtain ions of biomolecules from frozen water solutions (in the absence of solid surfaces) have largely been unsuccessful. If cryo-IR-SALDI analyte ions are preformed in the frozen solvent phase, as argued above, the question arises as to why the solid organic surfaces are required in order to observe them. The reason may be that the organic crystals are required to achieve charge separation, as discussed above. However, it may well be that ion desorption from bulk water ice is prevented also by very fast evaporative cooling or by the difficulty of depositing a sufficient energy density to achieve disintegration into mainly monomolecular species [45]. The presence of the organic crystals can have an effect on either of these potential problems.

### Conclusions

This work demonstrates a technique that reliably produces laser desorption mass spectra of proteins and peptides from frozen aqueous solutions using an IR laser. Desorption/ionization from the aqueous phase is made possible by the presence of organic crystals, added prior to freezing the solution. The analytical figures of merit for the new technique, referred to as cryo-IR-SALDI, are promising: A uniform sample preparation method can be used, and the upper mass limit is high; ions with masses beyond  $10^5$  Da were observed in this work. Mass spectra have been obtained with a sample consumption of about 1 femtomole of peptide or 10 fmole of protein. Compared with UV-MALDI on the same instrument, the mass

resolution for peptides was lower, and the mass resolution for proteins slightly higher. Significant future improvements to cryo-IR-SALDI seem possible. Higher mass resolution should be obtained on time-of-flight mass spectrometers with a more modern design, for example incorporating reflectrons and delayed ion extraction [46,47] and by solving the problem of surface charging in frozen samples. Improved mass resolution should also further increase sensitivity. Future investigations to more fully characterize matrix effects, such as the sensitivity towards electrolytes and detergents, and to determine typical minimum amounts of "real-world" samples will better define the analytical utility of cryo-IR-SALDI.

Cryo-IR-SALDI points to novel approaches in laser desorption ionization. There is extensive contact between the organic crystal surfaces and protein analytes in the suspensions used in the present work. This will tend to denature proteins and make it impossible to detect intact sub-unit proteins and non-covalent complexes. However, it may well be possible to "engineer" the cryo-IR-SALDI surfaces in order to optimize the desorption/ionization process. One can envisage, for example, maneuverable probes that have tips with such "designed" SALDI surfaces. Such probes would allow for the aqueous solution, before and after freezing, to be physically separated from the SALDI surfaces until the point of desorption. The chances of being able to reliably detect non-covalent complexes of biomolecules, that pre-exist in solution, would thus be maximized. Such probes would also allow for the interaction between the SALDI surfaces and the frozen aqueous phase to be spatially controlled. This, in turn, might allow for new types of ion microscopy, as well as in-situ detection of biomolecules in tissues.

41  
CHAPTER 2

REVIEW OF THE LITERATURE AND METHODS USED  
TO STUDY RHODOPSIN/TRANSDUCIN INTERACTIONS

Description of Signal Transduction in a Rod Outer Segment Cell

Figure 7 shows a pictorial schematic of the visual signal transduction cascade. Absorption of a photon and isomerization of rhodopsin's chromophore retinal, initiates the first amplification step of the light signal ---- rhodopsin/transducin binding. Each excited rhodopsin catalyzes activation of 600 transducin molecules/second at 22 degrees celcius (49) by catalyzing GDP release from the alpha subunit of transducin. The nucleotide free transducin then binds the much more cellularly abundant GTP. The transducin alpha subunit (Gt alpha) with GTP bound dissociates from the two other transducin subunits (beta and gamma), and goes on to activate a 3',5'-cyclic-GMP phosphodiesterase, which each catalyze the formation of several thousand 5'GMP/second from cyclic GMP. The decrease of cyclic GMP concentration which leads to the closure of  $\text{Na}^+/\text{Ca}^{+2}$  channels in the outer plasma membrane of the retinal roud outer segment, hyperpolarizes the rod cell membrane. The several stages of amplification leads to exclusion of  $\sim 10^7 \text{Na}^+$  ions/photon, and is the reason one photon can produce a physiologically measurable change in cellular current.

The rhodopsin-transducin coupling is an archetype for the large superfamily of GPCR-G protein systems in biology. Understanding the mechanisms of rhodopsin-

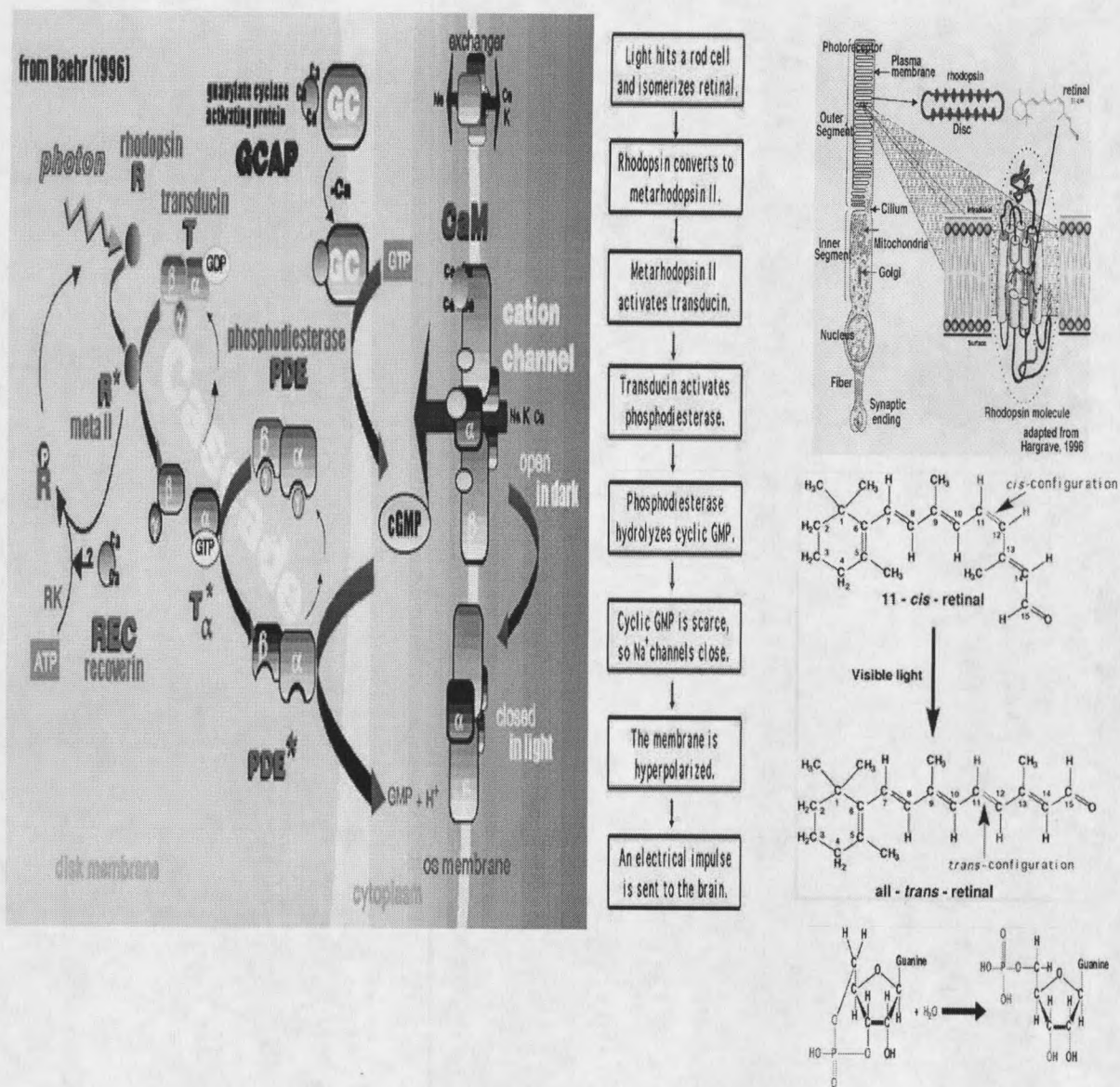


Figure 7. The light stimulated signal transduction cascade. Also shown are depictions of the location of rhodopsin in the rod cell, the cis to trans isomerization of retinal, and the hydrolysis of cyclic GMP.

transducin coupling is expected to also be valuable for understanding the coupling mechanism in a vast number of homologous systems.

### Relationship of Rhodopsin/Transducin System to other GPCR/G protein Systems

#### Rhodopsin dark structure and homology to other GPCRs

Homology predictions of the rhodopsin transducin interface concur with many of the mutagenesis studies. Figure 8 shows the evolutionary relationships of GPCR's based on sequence homology (50). Rhodopsin is a member of the Class A Rhodopsin like, family of seven transmembrane G protein coupled receptors (GPCR's). It shares approximately 30% sequence homology with other members of it's class. Figure 9, from Strathmann et al (51), shows the evolutionary relationship of G protein sequences. Transducin, the G protein (Gt) that binds to light excited rhodopsin binds, is most homologous (68%) to the Gi proteins which inhibit adenylyl cyclase. A snake diagram of rhodopsin in Figure 10A highlights mutational analyses of functional importance to rhodopsin activation of transducin. Recently, the crystal structure of dark-adapted rhodopsin has been solved to 2.8 angstrom resolution, and Figure 10B shows a backbone trace of the approximate dark adapted transmembrane disposition (52). Proteins with greater than 30% sequence homology typically have structures within 1 Angstrom RMSD (53). While both the dark structure of rhodopsin and the structure of Gt is known, neither the light adapted rhodopsin structure, nor the rhodopsin/Gt complex

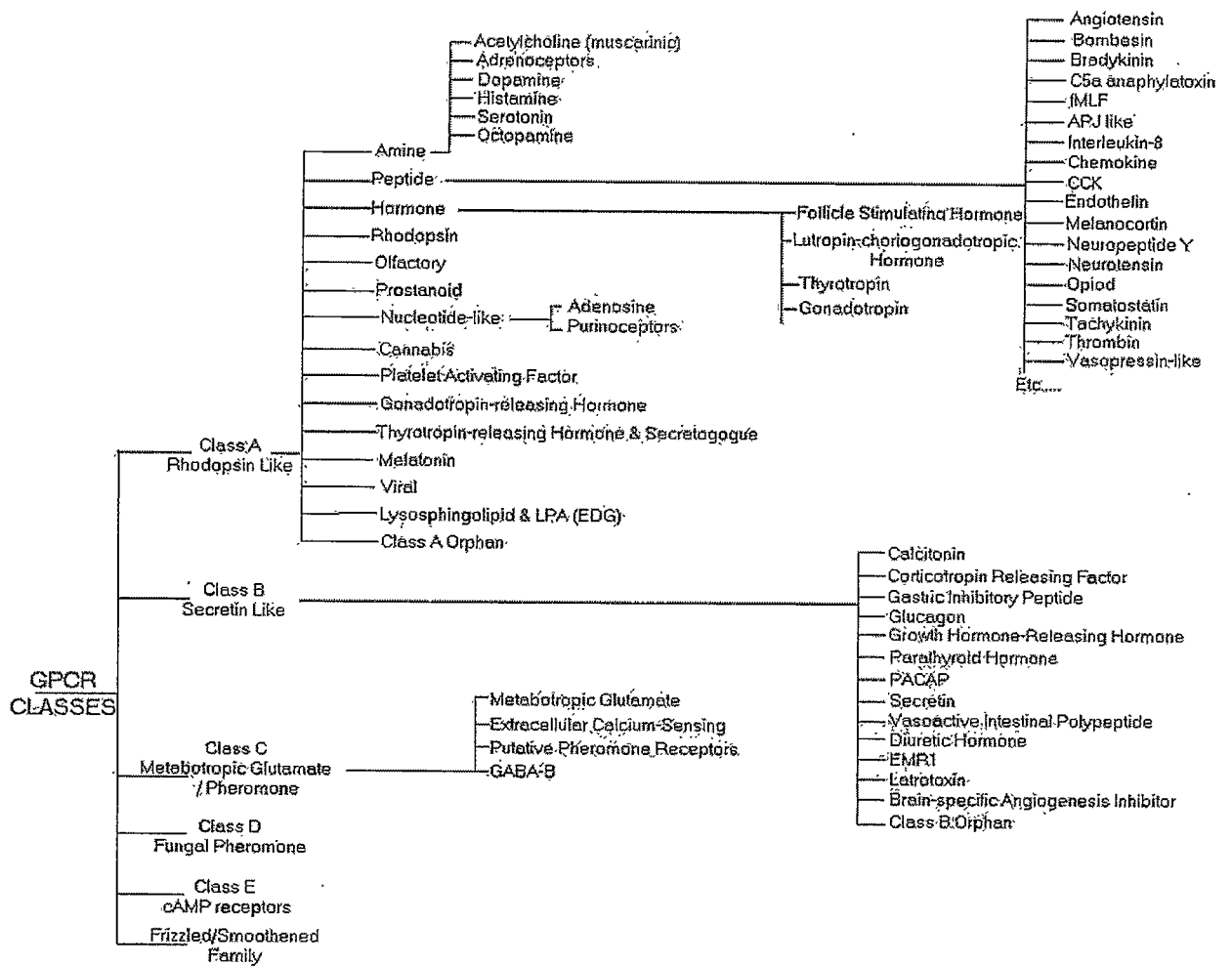


Figure 8. GPCR Evolution Tree

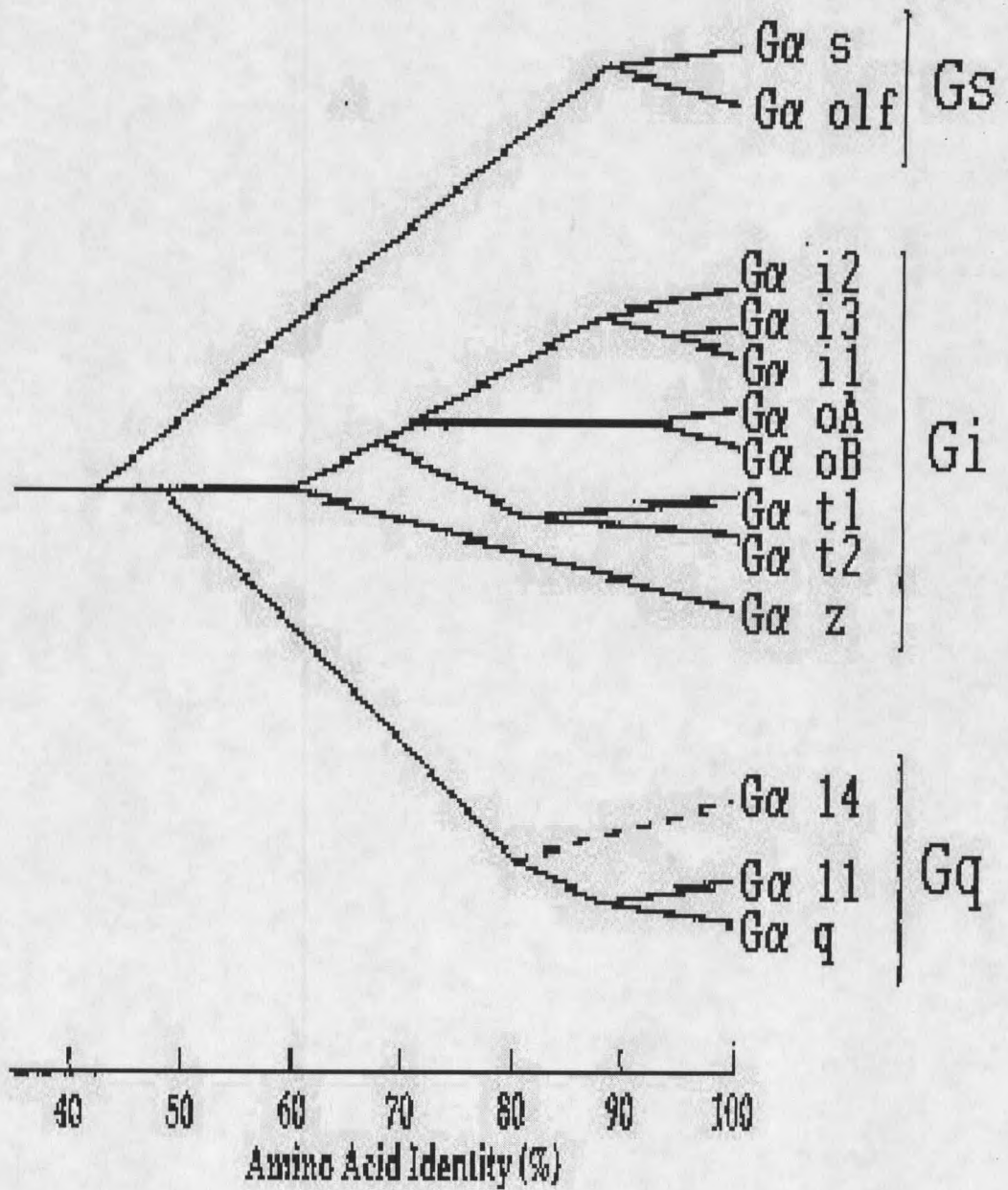


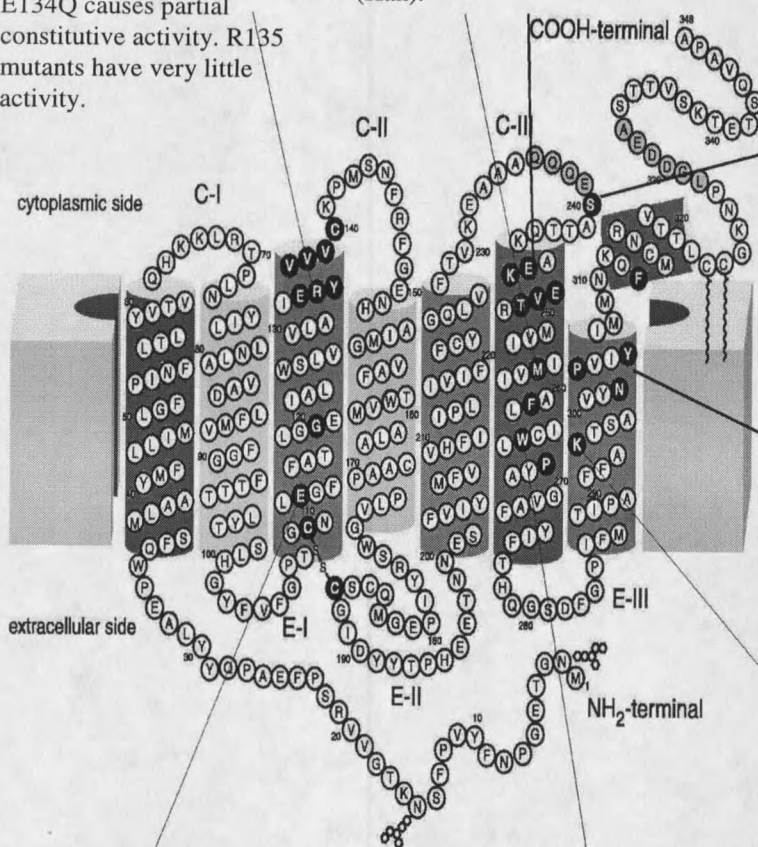
Figure 9. Relationships among mammalian G protein alpha subunits.

ERY is highly conserved in rhodopsin family.

Evidence presented that YVVV interacts with EKEVT of H-VI (Acharya). V138, E134, C140 are critical for full activation (Yamashita). E134Q causes partial constitutive activity. R135 mutants have very little activity.

M257Y opsin has 33% of WT rhodopsin activity (Han).

A spin label attached to V250C indicates Environment change upon Meta II formation (Dunham)



S240C + photo probe cross-Links to Gt alpha (Resek). Swapping C-III loop of Go Switches specificity (Yamashita)

NPXXY is highly conserved In all GPCR's. H-VIII above Was previously thought to be C-IV. N310S reduces activity to 39% of wild type (Marin).

K296 site of retinal Schiff's base attachment

G121 is the steric trigger of the 9-methyl of retinal. E113 is thought to be the counter ion to K296. E113Q opsin has 23% of WT rhodopsin activity (Han).

Beta-ion ring of photo-activatable retinal cross-links to W265 in dark state (Nakayama, Zhang, Borhan)

Figure 10A Snake diagram of rhodopsin (4). Grey scale residues were not located in the crystal structure.

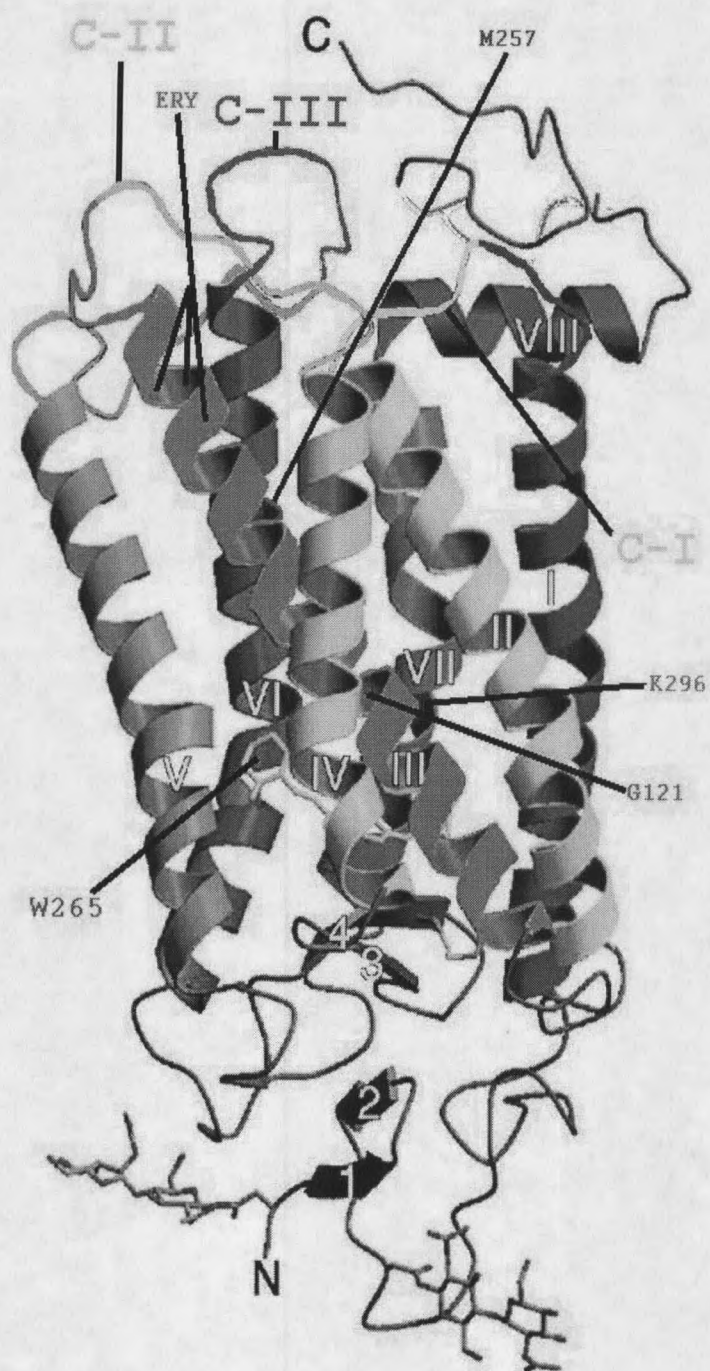


Figure 10B. Ribbon model of the crystal structure of dark-adapted rhodopsin.

has been solved. Using cDNA derived protein sequences of many GPCRs' and G proteins, Oliveria et al (54), Lithtarge et al (55), and Horn et al (56) attempted to define the residues that correlated with functional variation. Oliveira et al emphasized the importance of the conserved DRY motif (which is ERY in rhodopsin) near the cytoplasmic side of H-III in G protein binding. The authors proposed an "arginine switch" in which agonist binding favors movement of the arginine, conserved in H-III of all Class A rhodopsin like GPCRs, moves from a polar pocket in the transmembrane region to the cytosol to favor coupling to the G protein. Horn et al compared several GPCR sub-families within the Rhodopsin like, A Class. By looking at particular highly homologous families that all bound the same ligand, but bound different G proteins, they sought to see which amino acid residues that correlated with G protein selectivity. For example, Figure 11 (from Horn et al (56)) shows that Muscarinic m1, m3, and m5 receptors couple to Gq subtype, whereas, m2 and m4 couple to Gi/o. 24 positions correlated 100% with G protein coupling in muscarinic receptors. 18 are located in or close to the intracellular loops, mostly in the N- and C-terminal parts of the long third loop. 6 positions were considered false positives because they are located far from the intracellular compartment. Ten were confirmed by experimental data, 8 are putative candidates that have not yet been validated by mutational studies. Similar analyses were performed with the other Class A rhodopsin GPCR families, but with much less convincing results perhaps because there were fewer sequences to compare.

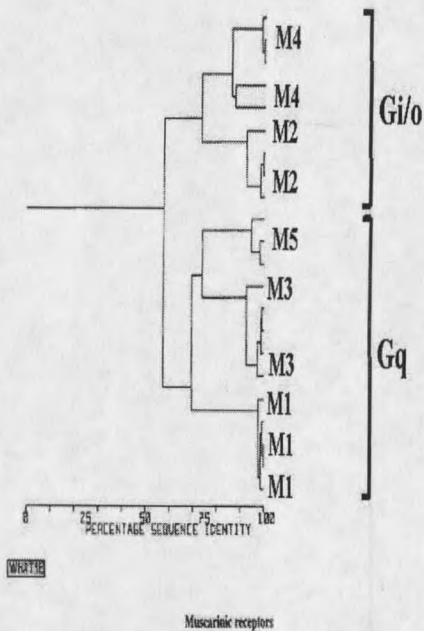
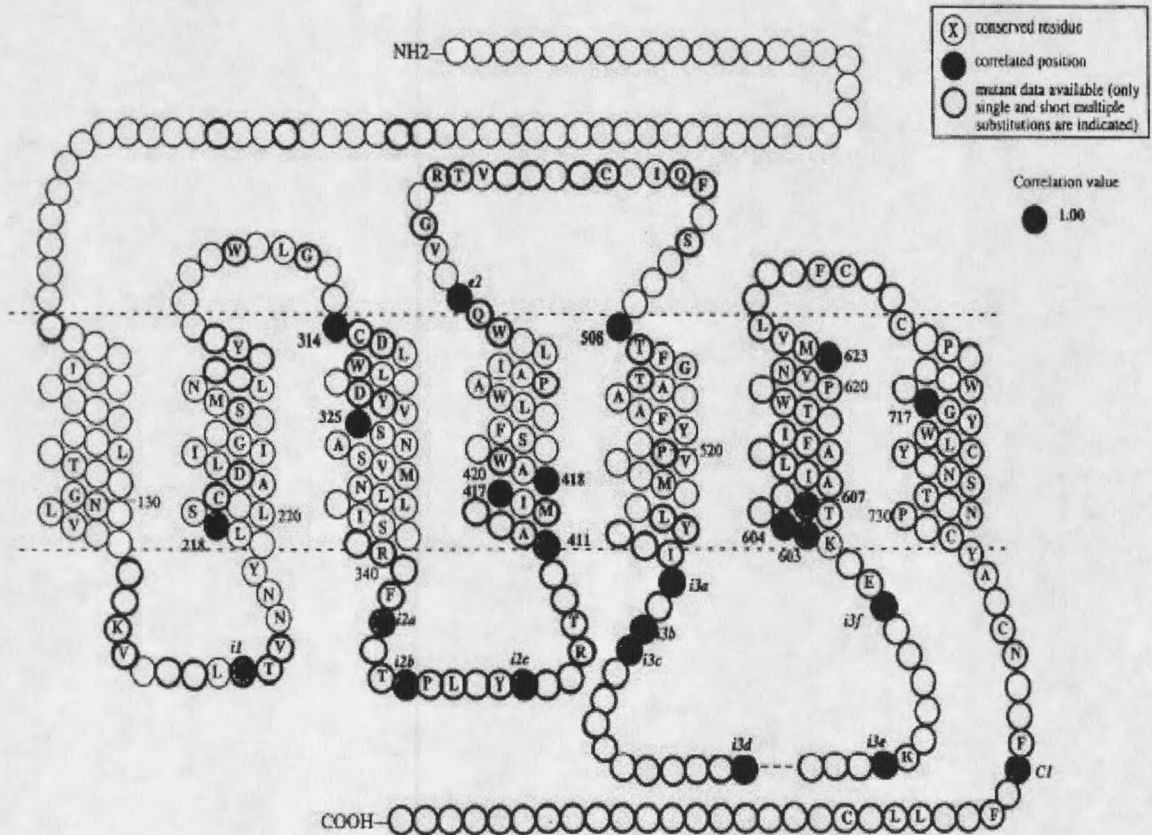


Figure 11. Muscarinic receptors M4 & M2 couple to Gi/o, and M5, M3, & M1 couple to Gq. Snake diagram below indicates the 24 positions near the cytoplasmic side (bottom side) that Horn et al [Proteins 2000] correlated with G protein selectivity.



Transducin structure and homology to other G proteins

Figure 12 shows the sequence of the alpha subunit of transducin with structural and mutational points of interest. Figure 13A shows a backbone trace of transducin with its beta-gamma subunits in back, and the alpha subunit in front. Figure 13B shows an expanded view of the alpha subunit. As highlighted in Figure 13B, the alpha subunit is composed of an alpha helical domain, and a GTPase domain, and the nucleotide is sandwiched between them in the interdomain cleft. Mutational studies have focused on the alpha subunit, since it is the site of nucleotide binding, although nucleotide exchange on the alpha subunit will not occur unless it is bound to the beta-gamma subunits (57-61). Lichtarge et al (55) used what they call Evolutionary Trace Analysis of 112 G alpha, 20 G beta, and 16 G gamma sequences to identify functional sequence variations in G proteins. They identified two surface clusters, A1 and A2 in the alpha subunit, that they attributed to sites of interaction with the receptor and effector. Cluster A1 consists of 17 residues stretching from the membrane face to the interdomain cleft. They include regions of the distal two thirds of helix alpha 5, the sixth beta-strand, the alpha 4/beta 6 loop, the N-terminal ends of beta 4, and beta 5, and the C-terminal tail. 9 of the 17 residues are GPCR class specific. The A1 cluster is thought to be the probable contact region for the GPCR. Cluster A2 of G alpha, comprising 32 residues (14 of which are class specific) interacts with G beta/gamma and probably with effectors as well. This prediction is confirmed by the published G protein holoenzyme structure. The interface of alpha to beta-gamma, defined as the set of residues in G alpha that lie within 4 angstroms of G beta-gamma comprise 16 of the 32 residues in cluster A2.

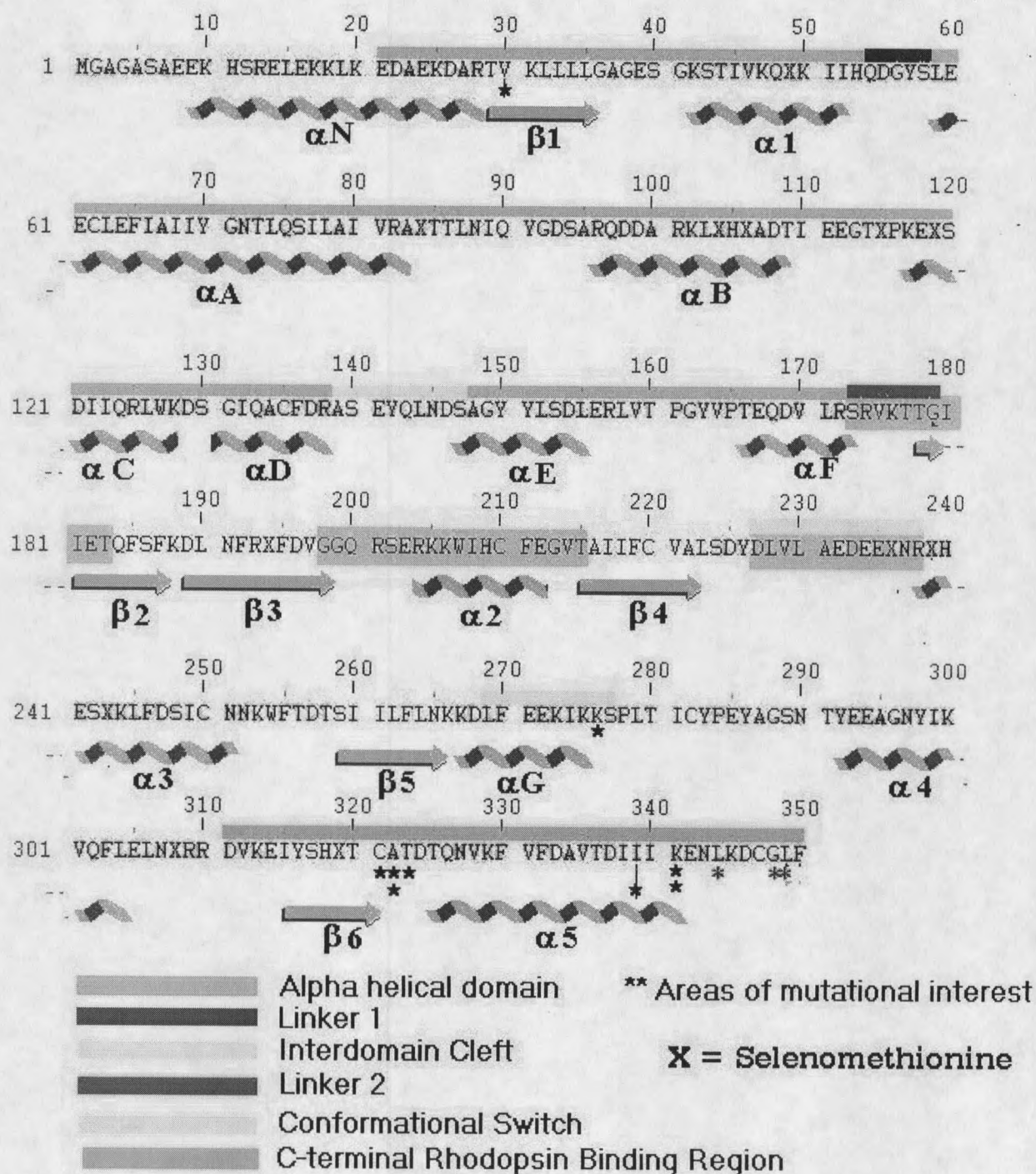


Figure 12. Sequence of the alpha subunit Gi chimera of transducin.

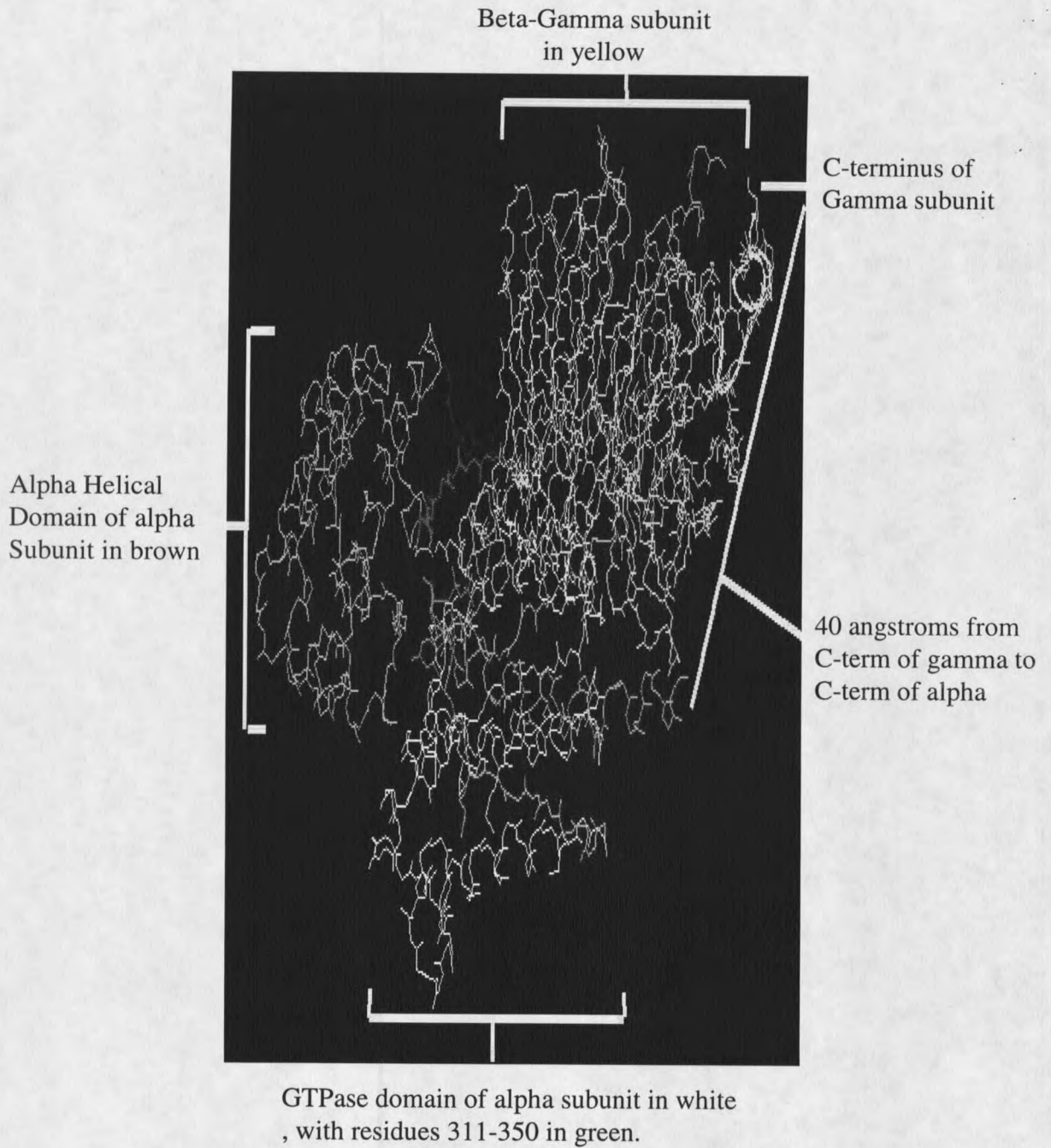
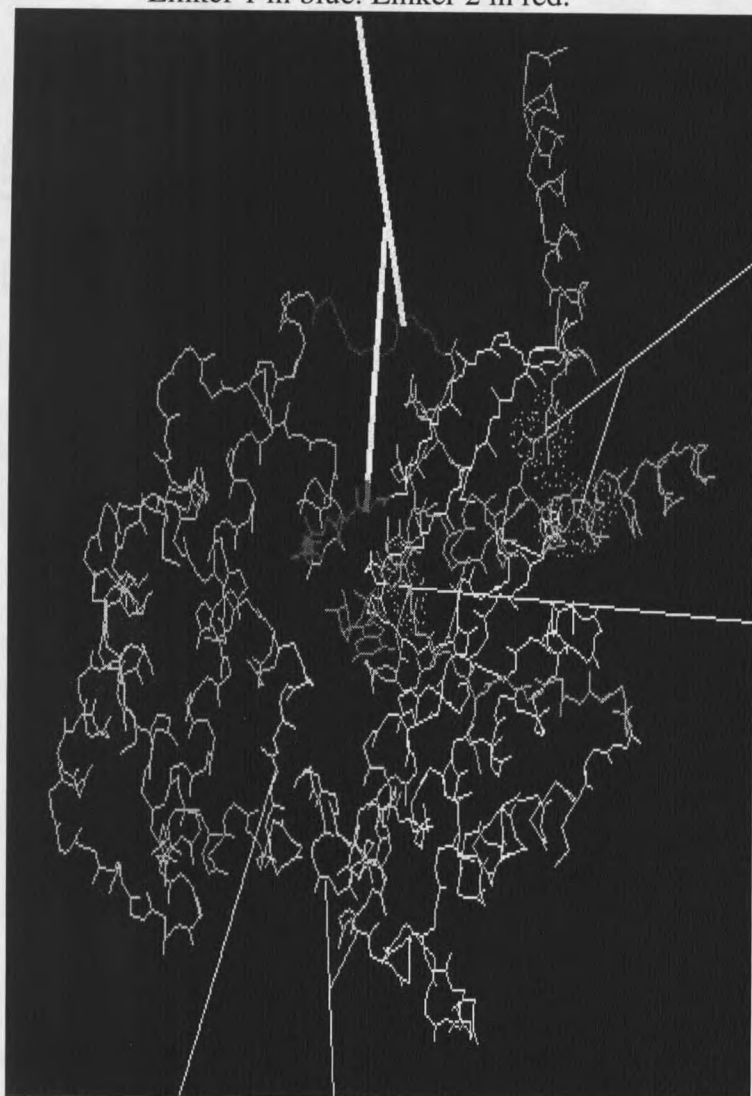


Figure 13A. Backbone trace of heterotrimeric transducin Gi chimera that was crystallized by Lambright et al [Nature 1996].

Linker 1 in blue. Linker 2 in red.



Mutations of V30 of N-term and I339 of C-term increase basal nucleotide exchange rate [Muradov].

Residues 311-350 in green are part of GTPase domain . C321, A322, and T323 contact the guanine ring (in pink). The white line points to A322, which is analogous to A326 of Gi1. The A326S mutant of Gi1 has a 250X increase in basal GDP nucleotide dissociation rate [Posner]. Peptides Ac311-329NH<sub>2</sub> and Ac340-350 stabilize Metarhodopsin II [Hamm] and block rhodopsin catalyzed nucleotide exchange [Kraft, Chapter 3].

Residues 139-147 of interdomain cleft of helical domain in yellow

Residues 227-238 and 269-277 of interdomain cleft of GTPase domain in yellow. K276E mutant has 10X increase in basal nucleotide exchange rate (Marin).

Figure 13B. Expanded view of transducin Gi chimeric alpha subunit.

Methods to Study Signal Transduction

The ability to obtain an X-ray or NMR structure depends for the most part on obtaining significantly large milligram quantities of very pure folded protein from its native tissue, or recombinantly from bacteria or insect cells. For structures of mutant proteins, to study correlations between sequence variations and function, this requires recombinant expression. Wild type transducin has proven impossible to express recombinantly in bacteria, whereas the 68% homologous Gi1 alpha is readily expressed in great quantities as a soluble folded protein. Skiba et al (62) used this as a strategy to get recombinant transducin to fold by systematic replacement of transducin regions, which inhibit proper folding, with Gi1 alpha, which are permissive for folding. Doing this were able to express large quantities of a Gt/Gi chimera that retained the functional characteristics of transducin ---- low basal guanine nucleotide exchange, and a high amplification (780X) in nucleotide exchange in the presence of light adapted rhodopsin. The structure depicted in Figures 6, and 7A & B is of this transducin chimera. Gt alpha residues 344-350 and Gt gamma residues 66-71 do not appear in the crystal structure, but were added to yield a more complete model. Crystal structures of wild type transducin alpha (purified from its natural abundant source in bovine retinas) with GTP-gamma-S, GDP, GDP and Mg<sup>++</sup>, GDP and AlF have also been solved, but a nucleotide free G alpha structure has yet to be reported.

The dark adapted structure of rhodopsin has only very recently been solved, ---- despite a large quantities of pure source of rhodopsin obtainable from bovine retinae. The

light adapted structure has not been solved presumably because of the difficulty in obtaining a single conformation of the light state. Expression of rhodopsin recombinantly has so far only produced quantities too small to make crystallization studies feasible. Rhodopsin mutants are usually expressed in COS cells where they are usually correctly folded, but are not expressed in high purity or in high quantities necessary for obtaining good crystals. Mutational studies of rhodopsin can be difficult to interpret because most of them have been designed without the aid of any GPCR crystal structures. Without crystal structures of the mutants, or at least of the wild type light adapted rhodopsin, an observer does not know if the mutation is "making or reporting the news". The dark adapted rhodopsin crystal structure is bound to lead to more focused design of mutational experiments. Despite the inability to obtain structures of mutants, mutational analysis has played a critical role in deriving the mechanisms of GPCR and G protein activation.

Biochemical and spectroscopic methods used on wild type protein or on mutants has provided the bulk of our present knowledge of the interactions responsible for the coupling of rhodopsin to transducin. These efforts can be categorized into four strategies. 1) Spectroscopic assessment of GPCR activation of the G protein using UV/VIS, light scattering, fluorescence, FTIR, and radioligand detection of binding. 2) Mutagenesis of select amino acid residues in the GPCR, and/or the G protein to determine their effect on G protein activation. 3) Chemical modification and/or cross-linking of the GPCR and/or G protein. 4) The use of peptides as probes of GPCR and G Protein function. Peptides derived from the G protein or GPCR can affect GPCR ligand binding, and GPCR catalysis of G protein radionucleotide binding, and therefore they also affect proteins

downstream of G protein activation. Examples of the strategies one and four are described in Figures 14 & 15 respectively.

### Spectral Characteristics of the Rhodopsin/Transducin System

Rhodopsin makes up 90% of the protein content of washed rod outer segment membranes (63). Multiple conformational states of rhodopsin were first characterized spectroscopically by changes in the visible/UV absorption spectrum (reviewed by (64; 65)) resulting from chemical tuning of the environment of its chromophore in the protein (11-cis retinal in the dark state absorbance max at 498nm, Ext Coef = 42,000 M<sup>-1</sup>cm<sup>-1</sup>). Retinal is formed from a vitamin A by oxidation of the alcohol to an aldehyde that attaches to lysine 296 in rhodopsin via a Schiff's base linkage. The purity of dark adapted rhodopsin is often assessed as the 280nm /496nm absorbance ratio. Protein impurities contribute to the 280 absorbance, but not the 498nm absorbance. Washed membranes typically have a ratio of 2 – 2.5, while the purest preparations have a ratio of about 1.6-1.65 (63). Productive rhodopsin/transducin interaction was first characterized (as depicted in Figure 14) by the radionucleotide ( [<sup>3</sup>H]GDP and [<sup>32</sup>P]GTP ) binding studies of ROS membranes by Godchaux & Zimmerman(66), and Fung & Stryer (67). Emies et al (68) confirmed the transducin binding by rhodopsin using a visible spectrum “extra Meta II” assay (as depicted in Figure 15. The Meta I state (Abs max 478) is in equilibrium with the Meta II state (Abs max 380nm).Binding of transducin

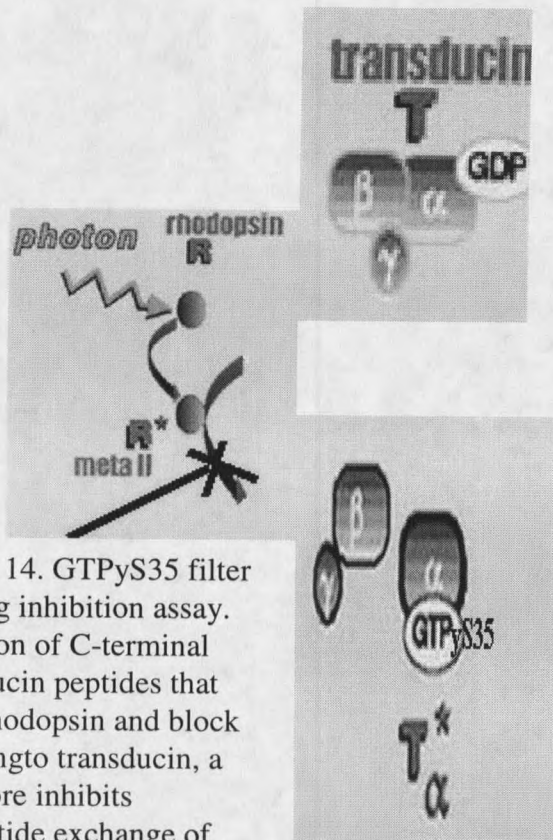
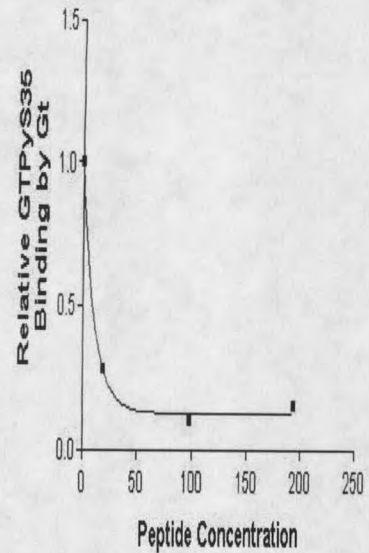


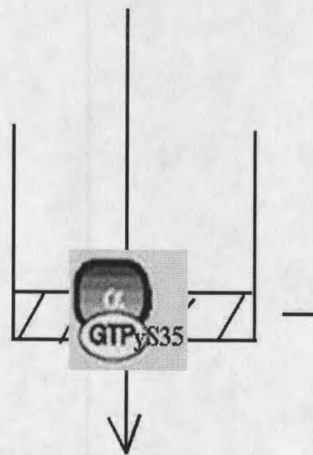
Figure 14. GTP $\gamma$ S35 filter binding inhibition assay. Addition of C-terminal transducin peptides that bind rhodopsin and block coupling to transducin, a therefore inhibits nucleotide exchange of GDP for GTP $\gamma$ S35 (non-hydrolyzable GTP analog) on transducin.

Example Curve of Peptide Inhibitor of Transducin binding



Solutions with and without various concentrations of competing peptides are all incubated with GTP-gamma-S35. After the incubation, solutions are suction filtered onto nitrocellulose filters, and washed with cold buffer to remove GTP-gamma-S35 not bound to transducin. Transducin with GTP-gamma-S35 bound sticks to the filter. Filters are dissolved in scintillation fluid and counted for radioactivity. As seen above, a plot of radioactivity vs peptide concentration yields an IC<sub>50</sub> for the rhodopsin transducin interaction.

Filter Binding



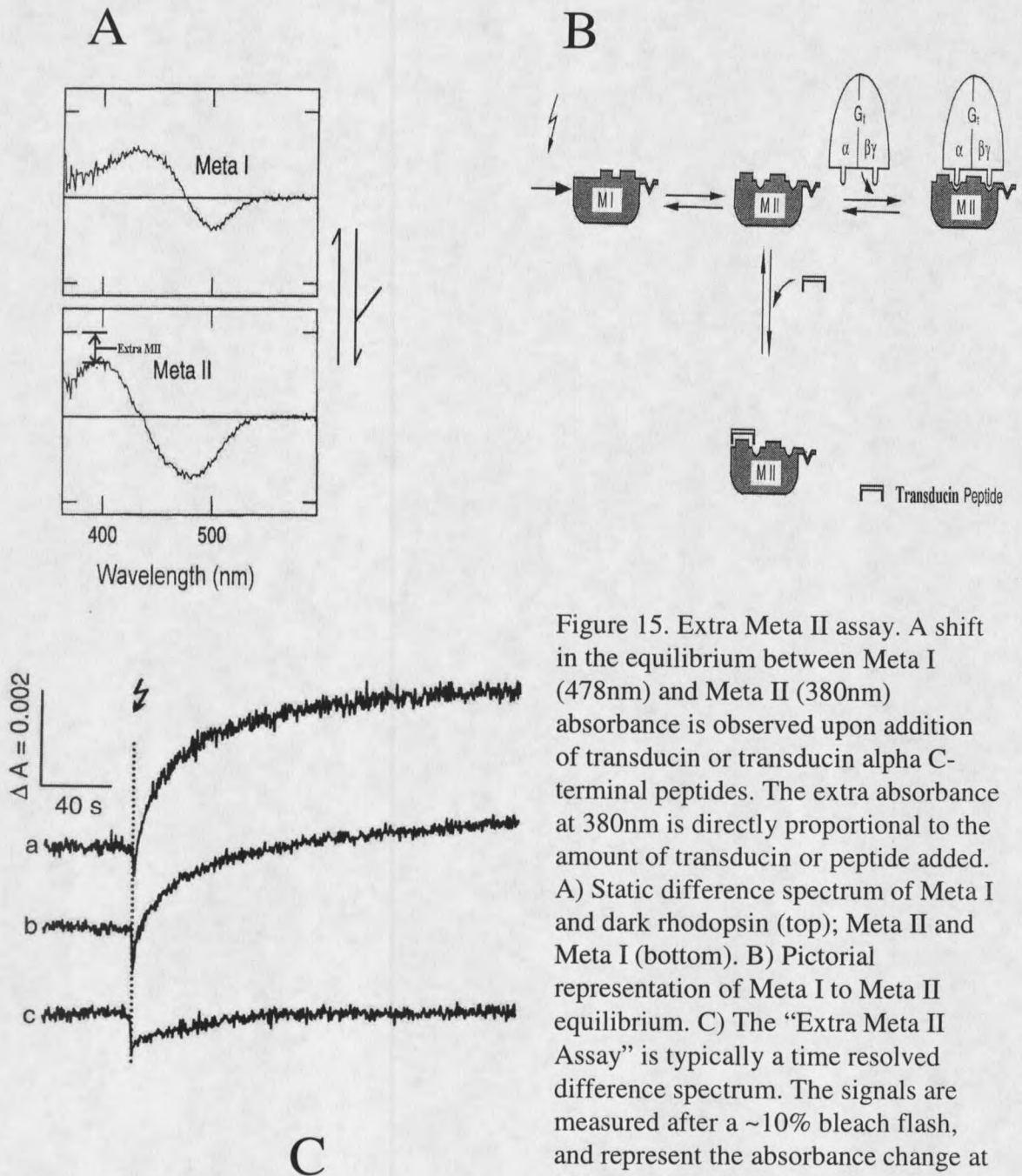


Figure 15. Extra Meta II assay. A shift in the equilibrium between Meta I (478nm) and Meta II (380nm) absorbance is observed upon addition of transducin or transducin alpha C-terminal peptides. The extra absorbance at 380nm is directly proportional to the amount of transducin or peptide added. A) Static difference spectrum of Meta I and dark rhodopsin (top); Meta II and Meta I (bottom). B) Pictorial representation of Meta I to Meta II equilibrium. C) The "Extra Meta II Assay" is typically a time resolved difference spectrum. The signals are measured after a ~10% bleach flash, and represent the absorbance change at 380 nm minus the absorbance change at 417 nm, as a function of increasing transducin or peptide. The abrupt decrease after the flash is due to the rapid formation of Meta II precursors.

to Meta II causes a shift of the Meta I / Meta II equilibrium detected by an increased absorbance of the Meta II state. Later reports also indicated that the Metarhodopsin II is the conformation that binds transducin and catalyzes nucleotide exchange (69). This binding event was also characterized by increases in light scattering of ROS membranes upon transducin binding (70; 71). Rhodopsin catalysis of nucleotide exchange, can also be characterized by increases in transducin tryptophan 207 fluorescence upon GTP binding (72; 73). Numerous studies have characterized the temperature, pH, ionic strength, and nucleotide dependence of these interactions (69; 73-79). Transducin and all G proteins have alpha, beta, and gamma subunits, of which the alpha is the most diverse. The alpha subunit releases GDP upon binding an activated GPCR, and then binds the GTP which is much more abundant in the cytosol.

#### Constitutive Activity of Rhodopsin and Transducin

A spontaneous exchange of GDP for GTP on the G alpha subunit takes place at very low levels the activated GPCR is not present, and the rapid exchange also requires G beta-gamma subunits. There are several classes of GPCRs based on sequence homology, with rhodopsin belonging to Class A which is the largest GPCR class. Rhodopsin and transducin are unique among the Class A GPCRs, in that both have a very low spontaneous or constitutive activity. In addition, opsin (rhodopsin without the chromophore retinal), can only activate transducin at very low levels. The low basal activity of wild type rhodopsin is an evolutionary adaptation of GPCRs unique to visual

receptors. Other GPCR's are 20-30% constitutively active (80) (the GPCR will catalyze nucleotide exchange without ligand binding).

Likewise G proteins other than transducin have a lower affinity for guanine nucleotides, and thus have a higher *basal* nucleotide exchange activity in the cytoplasm where GDP concentrations are much lower than GTP concentrations. The release of GDP is usually the rate limiting step in nucleotide exchange (76; 77). Light adapted rhodopsin catalyzes a 780 fold increase over *basal* transducin GTP binding. If ROS are urea stripped of their transducin and reconstituted with recombinant Gi, rhodopsin catalyzes only a 2-5 fold increase over *basal* Gi GTP-gamma35S binding. The initial rates of catalysis are 1304 umole/mole/s, ( $K_{app}$  0.095/min) for rhodopsin/Gi1, and 3798 umole/mole/s for rhodopsin/transducin ( $K_{app} = 0.3/\text{min}$ ) (62).

#### Role of Retinal in maintaining low basal rhodopsin activity

Reconstitution of opsin and 11-cis retinal in the dark leads to regeneration of the dark state of rhodopsin with equally low basal activity compared to the starting material, and has an absorbance max at 496nm. Maintenance of very low basal activity in dark rhodopsin is thought to be due to binding of 11-cis retinal (81) and also in part from a salt bridge between the Schiff's base K296 of helix seven (H-VII) and it's counterion E113 of helix three (H-III) (82; 83). As seen in Figure 16, photon absorption the 11-cis retinal isomerizes to trans retinal, and rhodopsin progresses in short intermediate steps from lumirhodopsin to the first long lived state, Metarhodopsin I (Meta I, absorbance max 478nm). E113 is then thought to accept a proton from the Schiff's base linked K296

breaking the salt bridge, and shifting the retinal absorbance maximum from 478nm to 380nm . Deprotonation of the Schiff's base and protonation of its counterion E113, and the resulting blue shift occur during the transition from the Meta I to Meta II conformation. Mutating K296 or its counter ion E113 to a neutral residue leads to constitutive transducin activation ( E113Q opsin has 23% of light activated wild type rhodopsin activity) (84)) (83; 85; 86; 86; 87).

#### Role of rhodopsin residues in maintaining low basal rhodopsin and transducin activity

Figure 10A summarizes the more important mutants described in this chapter. Examining mutants that cause opsin or dark adapted rhodopsin to activate transducin can lead to insight into identifying the dark state amino acid residues that maintain rhodopsin's very low basal activity, which are not directly involved in activation. All of rhodopsin's three cytoplasmic loops (C-I through C-III), and parts of their corresponding helices have been implicated as interacting with transducin. Parts of loops C-I, C-II, C-III, and all of what was thought to be C-IV were found to be helical in the new dark structure of rhodopsin (52) and for practical considerations, this discussion will refer to mutation site positions relative to the new dark structure, even though these sites may be altered in the light conformation.

Han et al (84) reported mutations of E113Q, E134Q, M257X (X = any amino acid except L or R), F261V cause constitutive activities in opsin of 23, 3, 32 (M257Y),

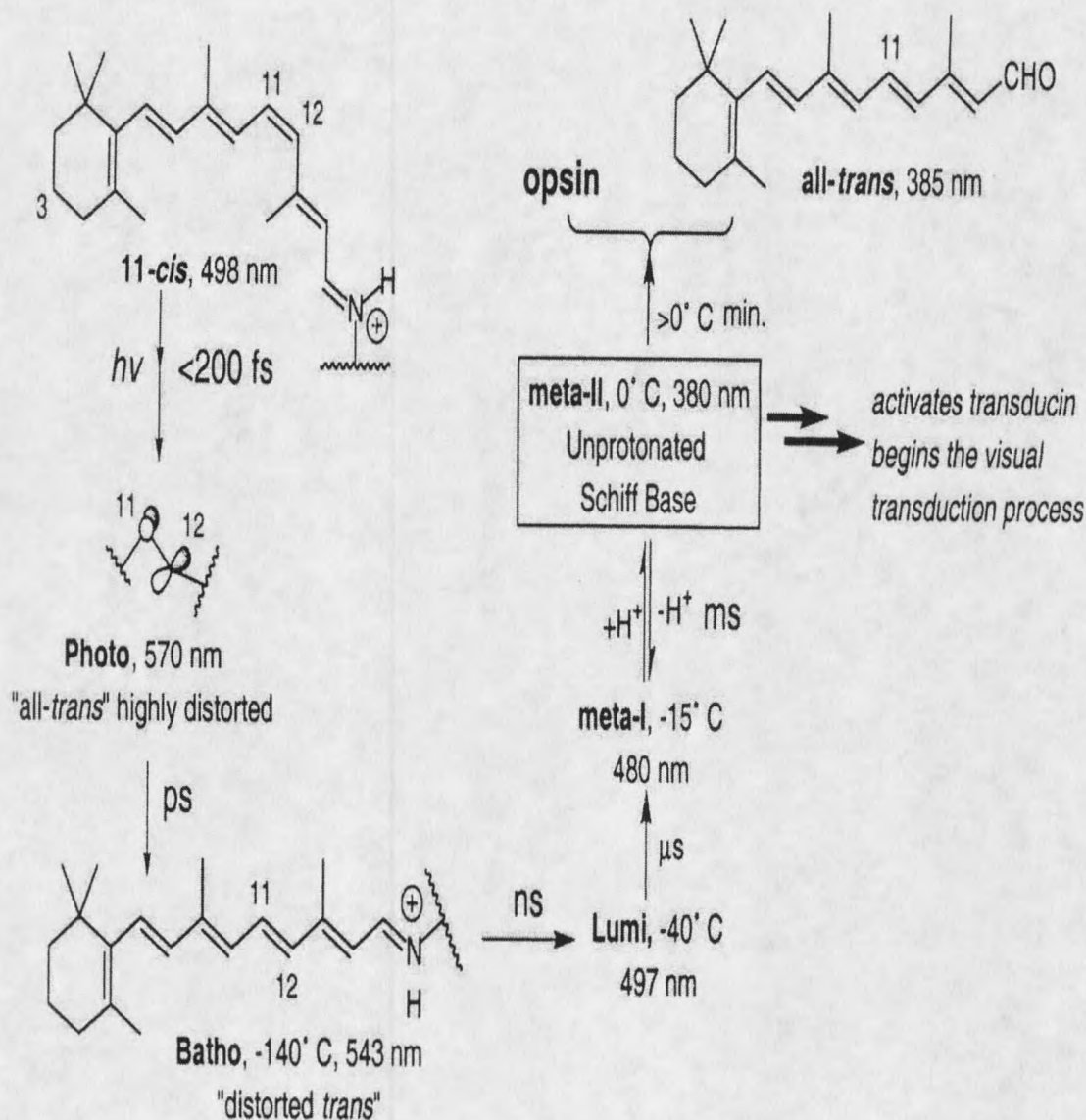


Figure 16. Spectroscopically detected intermediates in the photoisomerization of Rh. Initially, the 11-cis double bond is isomerized to a highly distorted trans intermediate (photo-Rh, cannot be isolated). Batho-Rh, a distorted 11-trans conformer, can be trapped at  $-140^{\circ}\text{C}$ , which upon warming to  $-40^{\circ}\text{C}$  yields lumi-Rh. A blue shifted intermediate (BSI) is in thermal equilibrium with the lumi-Rh intermediate but is not observed under cryogenic conditions; however, it can be observed with flash photolysis at ambient temperature. Meta-I-Rh, sequestered at  $-15^{\circ}\text{C}$ , is in equilibrium with Meta-II-Rh at  $0^{\circ}\text{C}$ . Therefore, it is possible to trap each intermediate at specific temperatures and study the orientation and movement of the chromophore with respect to the protein (199).

and 7.6 % of light activated wild type rhodopsin. Double mutant opsins, E113Q/M257A, E113Q/M257N, and E113Q/M257Y had 68, 74, and 81 % activity compared to wild type light activated rhodopsin.

Upon reconstitution with 11-cis retinal, all of the mutants' activity decreased to much lower levels, therefore, binding of 11-cis retinal can be an inverse agonist. Upon light activation of the mutants reconstituted with 11-cis retinal, the mutants M257A, M257C, M257F, M257I, M257K, M257L, M257Q, M257T, M257Y, E113Q, and E134Q had full activity compared to wild type.

All of the mutants (except M257L) had an increased ability to bind all trans retinal (ATR), reflecting the mutant opsins' conformational bias toward the active state. M257A, M257N, M257S, M257Y, and E113Q mutants in particular, had ~100% activity when reconstituted with ATR. When wild type opsin was reconstituted with ATR it had 14% of the activity of wild type opsin reconstituted with 11-cis retinal. This may reflect the reduced ability of wild type opsin to bind ATR.

The Meta I to Meta II transition is also accompanied by the uptake of a proton from solution by (74; 88; 89), although the function of proton uptake is not entirely clear. Many of the E134 rhodopsin mutants (in a conserved DRY of all GPCR's) of H-III are active in the dark state (84; 90; 91). Acharya et al reported the E134Q mutant to have a much higher opsin activity (46%), compared to Han et al's mutant E134Q opsin (3%). Han et al did report that the E134Q mutant had an increased ability to bind all trans retinal, with the ATR mutant having 51% of wild type activation. The E134Q mutant did not, however, have a decreased ability to bind 11-cis retinal as evidenced by its full light

activation compared to wild type. The E134D mutant has an ~50% decrease in transducin activation, and this decrease was independent of pH (92; 93). Acharya et al reported that while E134 to Q, I, and S increased the activity of opsin to about 50% of light activate wild type, they had little effect on the absolute rhodopsin light-activated rate, *and moreover*, E134 to L or F had no effect on opsin, dark or light activated rates of nucleotide catalysis.

#### Role of transducin residues in maintaining its low basal activity

Figures 12 and 13A & 13B summarize the more important transducin mutations discussed in this chapter. As mentioned before, transducin has a higher affinity for nucleotides than the 68% homologous Gi. Some mutations have been shown to increase basal transducin activity. Muradov & Artemyev (94) reported that coupling between the transducin alpha subunit's N- and C-terminal domains is thought to be partly responsible for transducins low intrinsic GDP/GTP exchange in unstimulated transducin. They demonstrated that mutational interruption of the interaction between V30 and I339 could cause increased basal nucleotide exchange.

Posner et al (95) reported the A326S mutant of Gi1 alpha (analogous to A322 in the CAT of Gt alpha) to have an ~250 fold increased dissociation rate of GDP, while having little effect on the affinity for GTP-gamma-S, or the intrinsic GTPase activity. The protein crystal structure was nearly identical to the wild type, with the mutant having a slightly less occupied GDP binding site. The authors argue that this mutant is an approximation of the receptor activated state of Gi alpha. Mutations of C325S of Go

alpha, and A366S of Gs alpha have similar effects (96; 97). The location of the analogous Gt alpha residue is marked in Figure 13B. Peptides from this region can bind and stabilize the Meta II state of rhodopsin (98), and the peptide N-acetyl-311-329-amide is able to block rhodopsin catalyzed nucleotide exchange with an IC50 of 400 nM (to be discussed in Chapter 3).

Very recently, Marin et al (99) did a mutagenesis study of the residues at the interdomain cleft of Gt alpha. It was originally hypothesized that a large rearrangement of the interdomain cleft would have to occur to induce GDP release/nucleotide exchange (100). Most mutants had minimal to no effect on basal Gt alpha nucleotide exchange. The charge reversal of K276E increased basal nucleotide exchange the most (10X). None of the mutants had an effect on the rhodopsin catalyzed maximal nucleotide exchange rate. The authors argue based on these results, and data not shown (of Gt alpha 5 mutants that caused >150 increase in basal nucleotide exchange), that rearrangement of the interdomain cleft is not the mechanism of receptor catalyzed increases in nucleotide exchange. They note that other monomeric G proteins that do not have a helical domain at all (that makes it look like a sandwich) release GDP more slowly than some heterotrimeric G proteins (101).

The A326S mutant of Gi does have a 250X fold increase in the GDP release rate, and its structure is nearly identical to the transducin GTP-gamma-S bound state, but it must be remembered that the crystal structure is probably the lowest energy state (it was crystallized with GTP-gamma-S bound), and presumably there is a higher energy intermediate nucleotide free state. As seen in Figure 17 from Posner et al, the A326S

mutant structure does show a loss interactions of C325 sulfur with the carbonyl of the guanine ring, of G45 amide with the alpha phosphate. Five other interactions are gained, and the sum of these interactions may favor the formation of the nucleotide free state.

### Activation of Rhodopsin and Transducin

#### Retinal Activation of Rhodopsin

As seen in Figure 10B, retinal attached to K296, is sandwiched between H-III and H-VI. The 9-methyl group of the retinal is thought to interact directly with G121 of opsin in the middle of H-III, and is known to be one of the crucial steric determinants of photoactivation (102). Removal of this group from retinal reduces the spectral shift from Meta I to Meta II and impairs rhodopsin catalytic efficiency to 8% of wild type (103). GPCR's other than rhodopsin, depend on a specific agonist ligand binding to stimulate formation of a active conformation that binds the G protein, releases its GDP, and catalyzes nucleotide exchange on the G protein. Retinal analogs have been synthesized with photo-activatable groups on the beta-ione, and these have been cross-linked in reconstituted wild type dark and light adapted rhodopsin (104; 105). Reconstitution of the retinal analog was about 50%, and about 20% of this cross-linked to dark adapted rhodopsin. In the dark and batho rhodopsin states, non-isomerizable retinal analogs the cross-linked mostly to W265 in H-VI, and to a lesser extent L266, as determined by Edmund sequencing.

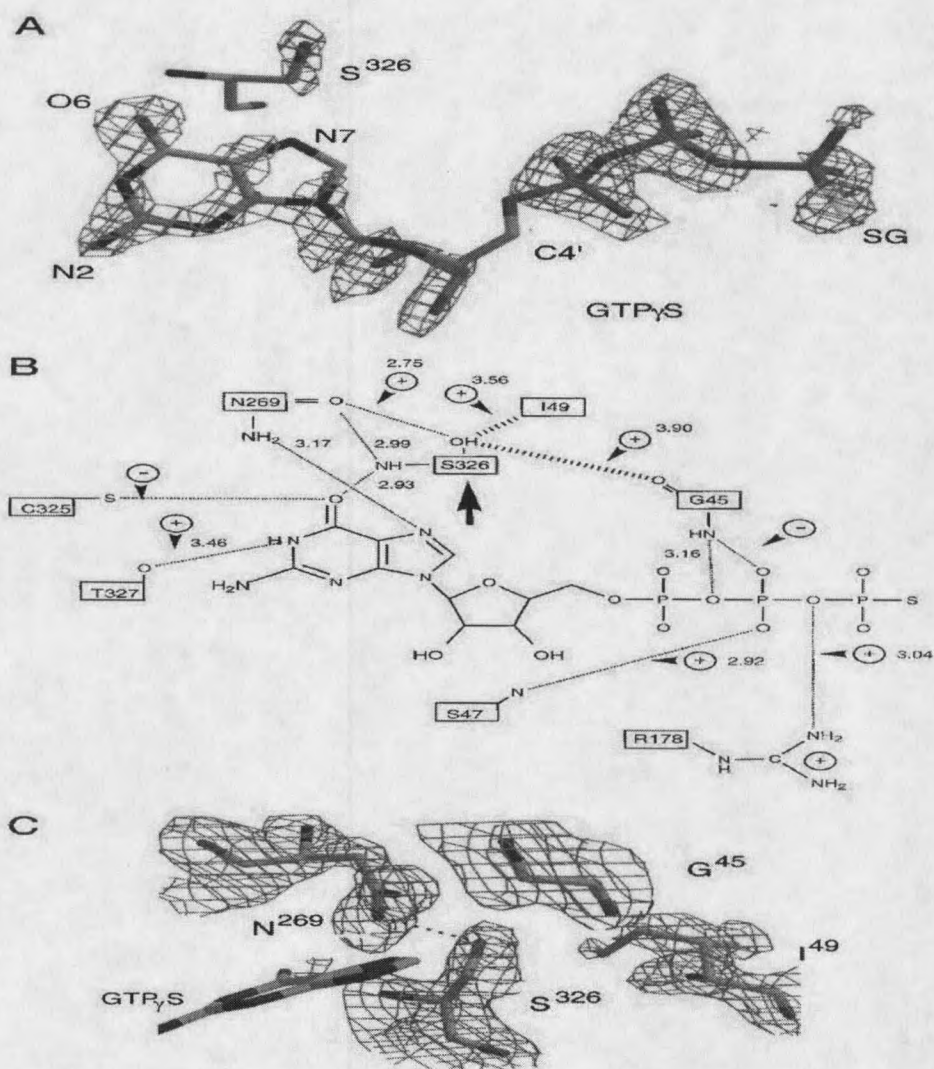


Figure 17. Structural Analysis of A326S Gi alpha-1 (95).

*A*,  $2F_o - F_c$  map calculated from the model for A326S  $G_{i\alpha_1}$ -GTPYS-

$Mg^{2+}$  after molecular replacement and rigid-body refinement of the search model. The map has been contoured at  $3.0 \sigma$  above the mean peak height. The electron density, colored in orange, indicates the location of the nucleotide and the mutant serine residue. The stick models indicate the position of the nucleotide and mutant serine in the refined model. *B*, noncovalent bonding interactions that have been perturbed in the active site of A326S  $G_{i\alpha_1}$ . Shown are hydrogen bonds (dashed lines) formed between protein residues and the nucleotide and van der Waals contacts (thick hash marks) between Ser326 and the protein that have changed in A326S  $G_{i\alpha_1}$ -GTPYS- $Mg^{2+}$  relative to the wild-type complex.

Interactions that have been gained (+) and that have been lost (-) in the mutant are indicated with the observed distances shown in *A*. Hydrogen bonds are defined as those interactions in which the donated hydrogen and acceptor atoms are separated by no more than  $2.5 \text{ \AA}$  and the angle subtended by donor, hydrogen, and acceptor atoms is greater than  $90^\circ$ . *C*, examples of the electron density in a  $2F_o - F_c$  map calculated from the refined model for A326S  $G_{i\alpha_1}$ -GTPYS- $Mg^{2+}$ .  $2F_o - F_c$  electron density map around Ser-326 contoured at  $1.5 \sigma$  above the mean peak height using phases derived from the final model. Electron density for GDP; only the purine ring is included in the schematic for clarity.

1994]. With light adapted rhodopsin cross-linking was observed at multiple sites in H-III(104), and at A169 in H-IV (105). Only 1.5% of the radioactivity was recovered in Borhan et al's (105) identification of A169 as the cross-linking site. Isolating sites of cross-linking, and chemical modification in rhodopsin is a difficult process because it requires digestion of rhodopsin and isolation of very sticky fragments. Co-elution of rhodopsin fragments is common in HPLC separation of rhodopsin digest peptide fragments (106; 107). The HPLC co-elution of rhodopsin fragments, the low recovery of radioactive cross-linked fragment yield, and the multiple sites identified call into question the correct identification of the cross-linking sites observed for the light adapted rhodopsin. Multiple cross-linking sites certainly are possible in the light adapted state. It will be of interest to see if future cross-linking attempts with transducin bound cause a preference of cross-linking to a single (or fewer) site.

#### Role of rhodopsin residues in activation

Some rhodopsin and transducin residues have been directly correlated with activation (See Figures 10A, 13B ). Mutation of these residues can lead to a decrease in transducin G-alpha-GTP formation. In rhodopsin (90; 108-110), the alpha1B-adrenergic receptor (111), chemokine receptor CX3CR1 (112), and muscarinic receptors (113; 114) R135 mutants of H-III virtually abolished G protein activation. The functional importance of this position is not universal to all GPCR's since other GPCR's are not as sensitive to substitutions at this position (115-117). Rhodopsin cysteine mutants of Y136, and V137-9 led to partial loss of transducin activation (118). Acharya et al (90) proposed

the YVVV of H-III and EKEVT of at the top of H-VI to form a pocket for the transducin C-terminal 340-350 peptide. Yamashita et al (93) were able to switch specificity of rhodopsin from Gt to Go by swapping the C-III loop with the C-III loop of the mAChR2, ETA, or ETB receptors. They also proposed that residues V138, E134, and C140 (which are opposite to R135, V139, and Y136 in helix C) were the most critical in maintaining full transducin activation.

Resek et al (119) made four single cysteine mutants H65C, C140, S240C, and C316. All other cysteines, except C110, 187 & 185 necessary for disulfide formation, were replaced with serines. These cysteines were derivatized by disulfide cross-linking to a tritiated photo-activatable probe. Only the derivatized mutant S240C from loop C-III was able to cross-link to Gt alpha upon exposure to UV light. The extent of cross-linking was very low (0.5% of the total radioactive label), and the site of cross-linking to Gt alpha was never located.

H-VII contains the site of retinal attachment to lysine 296. One might predict isomerization of 11-cis retinal to cause movement of H-VII relative to H-VI, and expose residues in H-VI critical to transducin activation. Disulfide cross-linking of 246C H-VI to 312C of H-VI, abolished transducin activation. A spin label at C316 of H-VIII, was reported to move apart from a label at position 65, at the amino terminus of transmembrane H-I, upon Meta II formation (120). Yet disulfide formation between C65 and C316, had no effect on transducin activation (121). A highly constrained rhodopsin, with the cytoplasmic ends of H-I & -VII, H-III & -V, and the extracellular ends of H-III

& -IV, and H-V & -VI disulfided, still retains 60% of the ability to activate transducin compared to wild type (122).

Farrens et al (123), using cysteine mutants and spin labeling deduced that Meta II formation involves an outward movement of H-VI away from H-III. Cross-linking of H-VI to H-III by cysteine mutant disulfides or metal chelating agents (121; 124) (123) (125) also abolishes transducin activation. An M257 substitution of H-VI with any amino acid except lucine and arginine causes constitutive activity (84). Dunham & Farrens (126) investigated residues nearby in H-VI to find residues involved in activation. They compared the ability of eight different cysteine mutants (near the residues at the top of H-VI in the Acharya study) to be chemically modified by the bulky PyMPO-maleimide probe and the environmentally sensitive fluorophore mBBr (monobromobimane). They found that dark adapted mutants K248C, E249C, T251C, R252C and I255C could react with PyMPO, but V250C, M253C, V254C, and I256C could not. The V250C showed a dramatic increase in reactivity with PyMPO in the light. K248C, E249C, V250C, T251C, and R252C were reactive with mBBr in the dark, but M253C, V254C, I255C, and I256C showed little or no reactivity. The mBBr modified mutant V250C was the only mutant that showed a large blue shift upon conversion from dark to Meta II state, corresponding to a dielectric constant change of ~44 to ~17 (more hydrophobic). Its fluorescence quenching by KI reversed from being unquenchable in the dark state to quenchable in the Meta II state.

Studies of the H-VIII have been contradictory. Osawa et al's (127) N310A, K311A, and Q312A point mutants had no effect. Cai et al's (128) Q312C mutant reduced

Gt activation to 88% of wild type. Marin et al's (129) N310S K311P Q312D, K311P, and K311W reduced Gt fluorescence activation to 39, 87, and 74 % of wild type. This region, from N310 to T320, has been determined to be the 8<sup>th</sup> helix in the dark structure, and spin labels attached to positions 316, and 313 in the middle of C-IV undergo increased mobility after photolysis (120). The rhodopsin derived peptide 310-321 from this region can cause red shifting and a 10% increase in transducin tryptophan fluorescence (130).

#### Role of transducin residues involved in activation/coupling to rhodopsin

Some of the C-terminal transducin residues previously discussed to affect the basal nucleotide exchange rate, are also implicated in coupling to rhodopsin. These will be discussed more in the next section focusing on peptides. The C-terminus of G alpha can be a key modulator of of GPCR specificity. Substitutions in G alpha expressed in human embryonic kidney cells demonstrated that mutants of glycine in the -3 position (relative to the C-terminus) suffice to switch the GPCR specificity of the G alpha q/alpha i2 chimeras. Certain mutations were able to switch the specificity of Gq to Gi2, Gq to Gs, and vice versa. The change in specificity, however, was only observed with particular GPCRs(131). Owasa et al (132) expressed transducin alpha subunit mutants invitro. Alanine mutants L344A, K345A, D346A, C347A, G348A, L349A, and F350A displayed 4%, 120%, 130%, 68%, 64%, 7%, and 70% of wild type binding. Mutations can lead to overall structural changes, and the binding of guanine nucleotide (a good test of structural integrity) can be measured by examining the resistance of the alpha subunit

to digestion by trypsin in the presence of GTP-gamma-S. G proteins have marked increases in resistance to trypsin digestion upon GTP-gamma-S binding (57; 58; 133; 134). These same mutants had 1%, 95%, 125%, 56%, 90%, 5% and 41% of wild type resistance to trypsin digestion. The highly conserved leucines were also more conservatively substituted with isoleucine, and these mutants L344I and L249I, demonstrated rhodopsin binding of 43 and 27% of wild type levels, and trypsin resistance of 69 and 50% of wild type levels.

#### Peptides as Probes of GPCR and G Protein function

There is an advantage to the use of peptides as probes of the wild type receptor/ligand interaction. This method does not suffer from the "making the news or reporting the news" problem associated with mutagenesis. Peptides (if derived from the proteins of interest) can give information about the specific residues responsible for receptor/ligand interaction. Peptides have been used to influence all stages of the signal transduction pathway. Measurement of the peptide influence at the first stage of signal transduction before the GPCR/ G protein interaction requires monitoring the ligand/GPCR interaction with radio or fluorescently labeled ligands (135-137). In the case of the visual pigment rhodopsin, peptide interference with rhodopsin coupling to transducin in the second stage can be measured using the UV/VIS "extra meta II assay" (68; 98; 138), the transducin fluorescence assay (129; 139; 140), or by monitoring GTP gamma S<sup>35</sup> binding, GDP<sup>32</sup> release, and/or P<sup>32</sup> release from GTPase activity (67; 90; 141; 142). Measurement of peptide interference of signal transduction after the GPCR/G

protein interface requires downstream monitoring of the G alpha/effector interaction or G beta-gamma/effector interactions (135-137).

A number of studies have implicated the C-terminus of the alpha subunit of the G protein as mediating signal transduction. Hamm et al (98) found bovine C-terminal G alpha protein derived peptides that could inhibit rhodopsin/transducin interaction and/or stabilize the active conformation of rhodopsin (mimic the effect of transducin holoprotein) as measured by the "extra Meta II assay". Various Gt alpha peptides spanning residues 8-23, 311-329, and 340-350 could inhibit rhodopsin/Gt interaction, but only peptides derived from 311-329 and 340-350 could independently bind and stabilize the MetaII state. The peptides N-acetyl-311-329-amide (Ac311-329NH<sub>2</sub>) and 340-350 had the most activity with IC<sub>50</sub>'s of 0.02 and 0.04 millimolar respectively for the rhodopsin/transducin interaction. The Ac311-329NH<sub>2</sub> peptide contains the CAT guanine ring binding region of transducin, and it is the only peptide known to both bind rhodopsin and interact with the nucleotide. Ruiz-Avila et al (143) found the bovine Gt alpha Ac311-329NH<sub>2</sub> peptide to be an inhibitor of taste cell membrane activation of rat transducin. Truncation of this peptide on either end lowered its activity, as did cyclizing it, or lengthening it. Different Transfer-NOESY NMR structures of the 340-350 peptide in complex with light activated rhodopsin have been reported (144-146). The alpha-5 helix of Gt alpha starts at threonine 325 and extends to various lengths in the reported crystal structures with the extreme C-termini disordered. One Gi alpha structure in complex with RGS4 (147) extends the C-terminal helix upto glycine 352 (analogous to G348 in transducin). The B-factors for the alpha carbons of I344, K345, N346, N347, L348,

K349, D350, C351, G352, L353, and F354 are 28, 26, 28, 31, 19, 19, 31, 37, 41, 30, 49 respectively.

Resenick et al (137) found two rat Gs derived carboxyl terminal peptides 354-372 and 384-394 could block beta-adrenergic stimulation of adenylyl cyclase in saponin-permeable C6 glioma cells, as measured by cAMP production, with IC<sub>50</sub>'s of 20 and 50 micromolar respectively. Both peptides could also mimic the effect of Gs to increase the agonist isoproterenol's affinity (decrease the K<sub>i</sub>) for the beta-adrenergic receptor, as measured by it's ability to inhibit receptor binding of the radioligand antagonist <sup>125</sup>I-pindolol (IPIN).

Martin et al (148) used combinatorial approach to find optimum bovine C-terminal Gt alpha peptides that mimic the extra Meta II effect of transducin binding to rhodopsin at low and submicromolar concentrations. Fourth round clones 8, 9, 10, 18, 23, and 24, as seen in Figure 18B and C had the most potency. Aris et al (149) explored these peptides further, and found that the K341L in 340-350 peptide analogs substitution had the greatest effect in producing a high affinity peptide analog to this region of Gt. Figure 19 combines Tables I – IV of Aris et al, summarizing the detailed peptide mutational analysis. Whereas some receptors activate multiple G proteins, A<sub>1</sub> adenosine receptors are preferentially coupled to Gi/o proteins. Gilchrist et al (135) found C-terminal Gi1/2 alpha and Gt alpha peptides to modulate agonist binding or antagonist-agonist competition using cells overexpressing A<sub>1</sub> adenosine receptors. Gi1/2 and Go alpha peptides 344-354 both inhibited binding of agonist [<sup>3</sup>H]N<sup>6</sup>- (cyclohexyl)adenosine (CHA) to A<sub>1</sub> adenosine receptor in rat cortical membranes with IC<sub>50</sub>'s of approximately 30















































































































































































